Seismological constraints on the down-dip shape of normal faults

Kirsty Reynolds and Alex Copley

COMET, Bullard Labs, Department of Earth Sciences, University of Cambridge, Cambridge, UK. E-mail: reynoldskirsty@mac.com

SUMMARY

We present a seismological technique for determining the down-dip shape of seismogenic normal faults. Synthetic models of non-planar source geometries reveal the important signals in teleseismic *P* and *SH* waveforms that are diagnostic of down-dip curvature. In particular, along-strike *SH* waveforms are the most sensitive to variations in source geometry, and have significantly more complex and larger-amplitude waveforms for curved source geometries than planar ones. We present the results of our forward-modelling technique for 13 earthquakes. Most continental normal-faulting earthquakes that rupture through the full seismogenic layer are planar and have dips of $30°$–$60°$. There is evidence for faults with a listric shape from some of the earthquakes occurring in two regions; Tibet and East Africa. These ruptures occurred on antithetic faults, or minor faults within the hanging walls of the rifts affected, which may suggest a reason for the down-dip curvature. For these earthquakes, the change in dip across the seismogenic part of the fault plane is $\leq 30°$.

Key words: Body waves; Earthquake source observations; Dynamics and mechanics of faulting.

1 INTRODUCTION

It is not known whether major earthquake-generating normal faults are dominantly planar, or whether the dip of the fault changes with depth so that they have significant curvature. Seismic reflection profiles and geological exposures commonly reveal both listric and planar normal faults in sedimentary units. There is ongoing debate regarding whether faults with steep surface dips flatten into subhorizontal detachment horizons around the depth of the brittle-ductile transition (e.g. Velasco *et al.* 2010). High-resolution bathymetric studies have revealed in great detail the corrugated, domed footwalls exposed in oceanic core complexes, but the geometrical evolution of these structures, and whether or not they slip in earthquakes, remains enigmatic (Escartín *et al.* 2008; MacLeod *et al.* 2009; Smith *et al.* 2014). The loss in resolution of geodetic techniques (e.g. GPS and InSAR) at depth, together with the non-uniqueness involved in inverting surface measurements for fault geometry and slip, means that it is difficult, using geodetic techniques, to determine the down-dip shape of seismogenic faults, particularly at the depths at which earthquakes nucleate. In this paper, we present a seismological technique for constraining the down-dip curvature of active normal faults. The advantage of using seismology is that it sheds light on the shape of the seismogenic part of the fault at the time it was active, and the technique is only sensitive to the parts of the fault that are important in generating earthquakes.
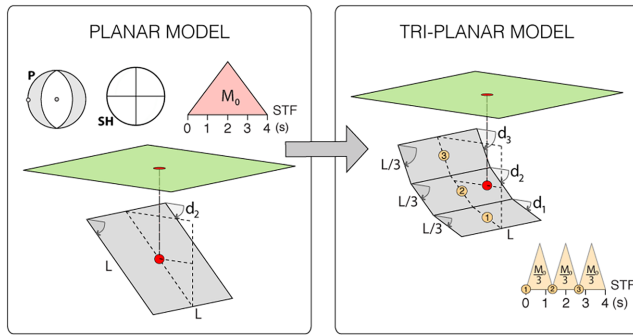
The wider implications of this work lie in several areas. First, normal fault curvature controls the geometry of basins and affects mechanisms of crustal thinning. For example, curved faults bounding regions which deform internally can accommodate significantly more extension than a series of planar faults bounding rigid crustal blocks (Jackson & McKenzie 1983; Jackson & White 1989). Second, the processes that initiate, drive, impede and finally stop earthquake ruptures are intrinsically linked to the physical attributes of faults (e.g. Sibson 1985; Scholz 1998), therefore knowledge of the shape of faults is important in investigations of fault rheology and mechanics. Third, the down-dip shape of normal faults has implications for assessing earthquake hazard, from the perspective of the location of energy release and the down-dip width of fault available to rupture.

First, we discuss our approach and model set-up, and how our method differs from that of Braunmiller & Nábělek (1996), on whose work we build. We then present a synthetic example to highlight the features of teleseismic waveforms that are indicative of the presence or absence of down-dip curvature. Finally, we describe the application of our method to a catalogue of continental and oceanic normal-faulting events, and present the results of the modelling along with a discussion of the constraints on the down-dip shape of the fault for each earthquake. Though we focus on normal faults, our technique is equally applicable to thrust earthquakes.

2 DATA AND FAULT MODELS

If an earthquake occurs on a fault plane with down-dip curvature, as the rupture proceeds through time and advances across the fault surface, different portions of the fault, which have different dips, will contribute to the signal recorded at a seismometer. If the rupture is of sufficient duration then the moment contributions from different parts of the fault plane, which contain information about the source geometry, are separate enough in time to be detected in seismic

Figure 1. Setup of tri-planar model geometry. Left: Initial planar model. For real earthquakes, the moment obtained for the point-source centroid (red dot) parameters is used to estimate the dimensions of a planar rupture patch of dimensions $L \times L$. Right: We use three-subsource models to simulate curvature: the planar rupture is broken into three rectangular patches, of dimensions $L \times \frac{L}{3}$, and a subsource centroid (numbered orange dots) is located at the centre of each. The relative timing of each subsource is determined by the size of the estimated rupture plane and a rupture velocity of $2.5\,\mathrm{km\,s^{-1}}$. The length of the source time function (STF) for each subsource (orange triangles labelled with numbered orange dot) is constrained so that the overall duration of the three-subsource event is the same as the length of the source time function obtained for the point-source inversion (red triangle).

waveforms. We exploit this complexity in the waveforms in this study.

We define down-dip fault curvature as the difference in dip between the upper and lower portions of the fault. A listric geometry, that is, decreasing dip with increasing depth, is defined as having negative curvature; a convex-up surface has positive curvature; and a plane has zero curvature. A curved surface can be approximated by a series of connected planes with different dips. For simplicity, and building upon the work of Braunmiller & Nábělek (1996), we model earthquakes using three subsources (Fig. 1). In this model, the rupture surface is approximated by three planes (tri-planar), and the subsources are offset in time and space, to represent the progress of the rupture through different parts of the fault.

Our study is restricted to events with magnitudes $>M_\mathrm{w}$ 5.5, below which we commonly do not see clear waveforms in broadband seismograms, and $<M_\mathrm{w}$ 6.5, above which the waveform complexity resulting from the rupture of multiple fault segments results in trade-offs with the fault geometry. Unlike field-based, InSAR or seismic reflection studies, our resolution is not limited by the depth extent of the rupture, or by geographic considerations (such as site access, errors due to topographic or meteorological effects, or whether the epicentre is on land or under the oceans).

The seismological technique we present is a forward-modelling method, based on the comparison of recorded waveforms with synthetic waveforms for tri-planar faults with planar and curved geometries. To construct the geometry of the three subsources for the tri-planar models, we estimate the dimensions of the rupture plane using the seismic moment of the centroid solution and fault scaling laws (as described below). For real earthquakes, we invert for these centroid parameters using *P*- and *SH*-waveform inversions, using the MT5 programme of Zwick *et al.* (1994) and McCaffrey *et al.* (1991) (discussed further below). For the synthetic earthquake, discussed in the next section, the value of the moment (and other source parameters) is chosen to be representative of the real earthquakes that we investigate. We refer to this initial centroid solution, on which the tri-planar models are based, as the planar model or single-plane solution. We estimate the dimensions of a square fault

plane using the seismic moment and a displacement-to-length ratio of 5×10^{-5} (Scholz 1982). This rupture plane is broken into three rectangular patches of length, L, and down-dip width, $\frac{L}{3}$ (Fig. 1). The centroids of the respective subsources are positioned at the centre of each subplane, and each subsource has a moment of $\frac{M_0}{3}$.
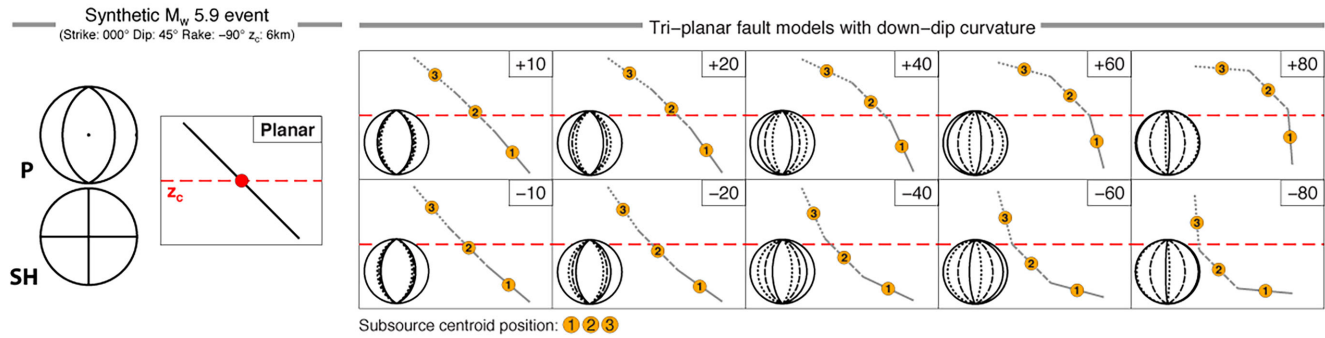
The relative positions and depths of the three subsources are recalculated for each degree of fault curvature that we model, while enforcing that the combined parameters of the three-source models average to the centroid solution, and that the structural contiguity of the fault model is maintained. As we prescribe each subsource with the same moment, the moment-averaged source parameters are also the same as the centroid solution. These steps ensure that our models are of physically plausible fault ruptures that are consistent with the overall centroid parameters of the events.

All subsources have strike and rake fixed to that of the centroid solution. The dip of the middle subsource is fixed to that of the centroid solution. To simulate down-dip curvature, the dips of the upper and lower subsources are varied in tandem, such that the average dip of the tri-planar model is the same as for the single-plane solution. The degree of curvature is the difference in dip between the upper and lower subsources ($-80°$ is very listric, $+80°$ is very convex-up). Dips are altered in $5°$ increments, resulting in models at $10°$ intervals of curvature, up to a maximum degree of curvature where the dip of the upper or lower subsource approaches vertical or horizontal.

Rupture of a curved surface is simulated by setting a time delay between subsources. We assume rupture nucleates at depth (initiating with the deepest subsource, S_1) and propagates upwards. We show in Appendix B in the Supporting Information the effects of rupture propagating from the surface downwards. The time delay between subsources is calculated using the model geometry and assuming a rupture velocity, v_r, of $2.5\,\mathrm{km\,s^{-1}}$. Each subsource has the same source time function, defined by a single triangular element, the duration of which is set so that the overall duration of the tri-planar event matches that of the centroid solution. We carried out synthetic tests (Appendix B in the Supporting Information) that show that variations in the timing of moment-release (due to our choice of rupture velocity and source time function parameters) have only a minor effect on the waveforms compared to changes in the down-dip geometry, and that our assumptions therefore do not affect our ability to resolve down-dip curvature.

2.1 Previous work

Braunmiller & Nábělek (1996) also used teleseismic body waveform data to examine the fault geometries in 6 normal-faulting earthquakes in Greece and western Turkey. They used three-subsource models to produce synthetic waveforms for rupture on faults with down-dip curvature, and found that *SH* wave shapes and polarities were strongly affected by down-dip curvature when observed at teleseismic stations lying approximately along-strike of the event. We build on their work to produce a new set of synthetic waveforms and present a technique for both identifying and constraining down-dip curvature from teleseismic data. We replicated the synthetic study of Braunmiller & Nábělek (1996) using the MT5 programme of Zwick *et al.* (1994) (which is detailed in Appendix A in the Supporting Information), and our method reproduces the differences in amplitude and polarity in the initial parts of *P* and *SH* waveforms between a planar rupture model and a curved fault plane (with $40°$ listric curvature) that they observed. We improve upon the study of Braunmiller & Nábělek (1996) by investigating the effects of the choice of model rupture velocity, source duration

Figure 2. Geometry of synthetic M_w 5.9 normal-faulting event and curvature models. Left: Red dot marks the point-source location (centroid) of the synthetic earthquake at a centroid depth, z_c, on a cross-section perpendicular to the event strike. The source parameters are shown above and the *P* and *SH* focal spheres are to the left. The point-source event is envisaged to occur on a planar fault surface with the same parameters as the source centroid (which we later refer to as the planar model, or single-plane solution). The centroid sits at the centre of this fault plane (black line). Right: Tri-planar models are generated by splitting the single-plane solution into three equal-sized rectangles, the dips of which are varied in order to simulate curvature. The cross-sections are perpendicular to strike and show the down-dip geometry of the tri-planar models in grey, relative to the single-plane solution centroid depth (dashed red line). Rupture of a tri-planar fault model is simulated using three point sources (subsources) with $\frac{1}{3}$ the moment of the single-plane solution, which are offset in space and time from each other. In the model rupture propagates from the bottom up, so the first subsource (1) is the deepest, the last (3) the shallowest. The location of each subsource centroid (orange dot) is at the centre of each of the three rectangular planes. Each cross-section is labelled with the amount of model down-dip curvature (difference in dip between the upper and lower planes) on the top right. On the bottom left, each cross-section has a *P* focal sphere showing the nodal planes of subsource 1 (solid), 2 (dashed) and 3 (dotted).

and propagation direction, which we describe in Appendix B in the Supporting Information. Different to Braunmiller and Nábělek, we also include the important and high-amplitude depth-phases (i.e. near-source surface reflections) in our synthetic waveforms, and we prescribe the subsource parameters such that our curved fault models are consistent with the centroid solution obtained through body waveform inversion.
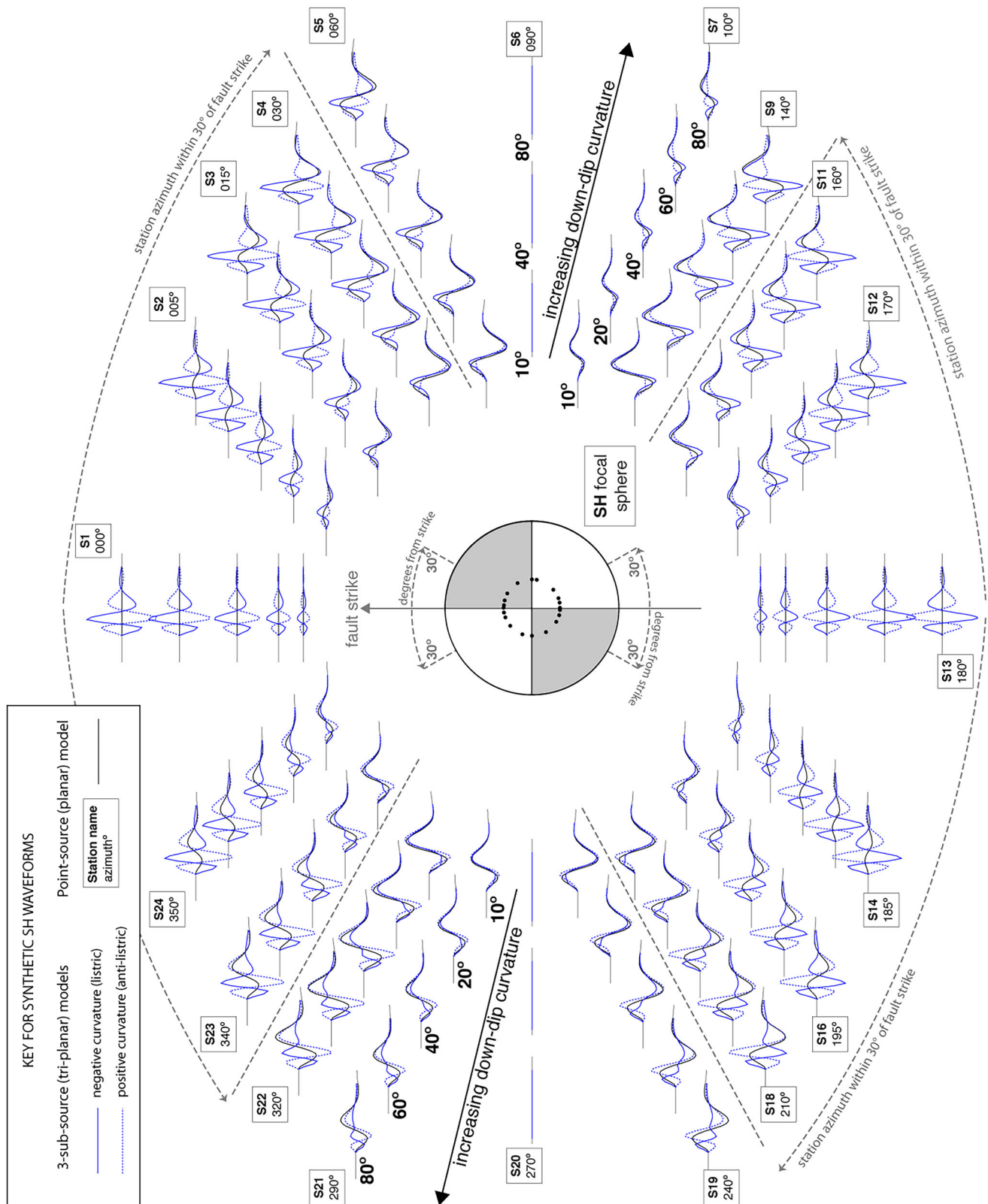
3 SYNTHETICS

We examine the effect on *P* and *SH* waveforms of changes in the down-dip geometry of a synthetic M_w 5.9 normal-faulting event, by computing synthetic seismograms for a suite of tri-planar models covering a $-80°$ to $+80°$ range of curvatures (Fig. 2), using the MT5 algorithm of McCaffrey *et al.* (1991) and Zwick *et al.* (1994). The synthetic stations were chosen to represent the typical epicentral distance ranges of teleseismic data used in body waveform inversions, and the magnitude of the synthetic earthquake was chosen to be similar to the real events discussed later. Figs 3 and 4 compare the synthetic *SH* and *P* waveforms for a planar fault model, with those for curved fault models at $\pm10°, 20°, 40°, 60°$ and $80°$ curvature. We investigate how waveform amplitude and complexity is affected by fault geometry and station location, and discuss the implications of our results for examining real data.

3.1 Synthetic waveforms

The synthetic seismograms at stations within $\sim30°$ of fault strike have significantly more complex *SH* waveforms for all curved fault models than for the planar case, even those with only $\pm10°$ curvature (Fig. 3). The *SH* waveforms at these stations also have much higher amplitudes for curved models, and along-strike nodal stations (stations S_1 and S_{13}) show waveforms whereas none are present for the planar model. These effects are more pronounced for models with greater curvature. At stations with azimuths at high angle to strike, *SH* waveforms for curved models are not as complex, and have similar amplitudes to (and are harder to distinguish by eye from) those for the planar fault model. However, for models with
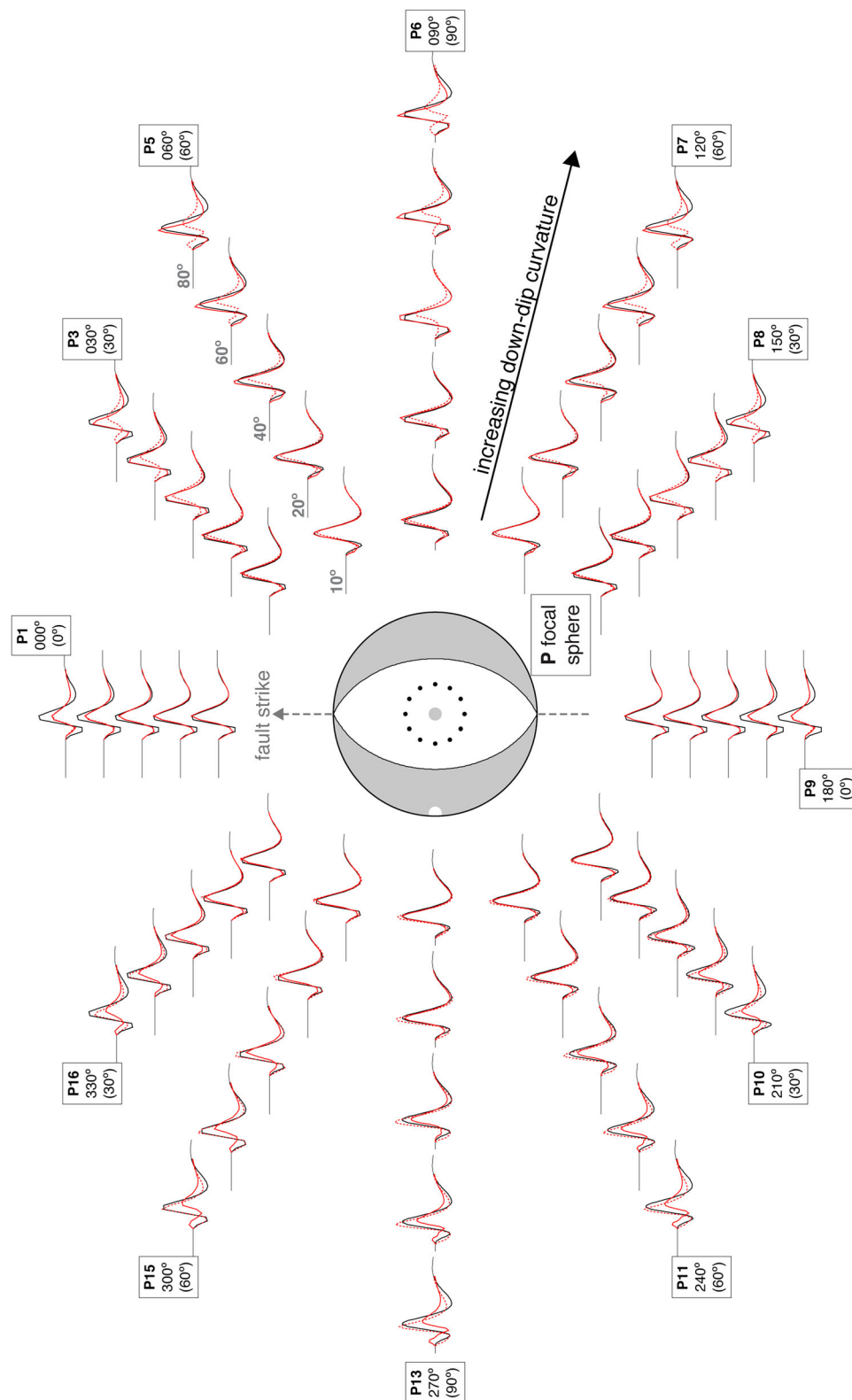
high curvature, the dip of the lowermost plane (subsource S_1) may be high or low enough that the nodal plane for this subsource lies on the opposite side of where these stations plot on the focal sphere, that is, the station projects to a different quadrant of the *SH* focal sphere. In this case the *SH* waveform shows a small amplitude peak with the opposite sign to that of the waveform for the planar model (Fig. 5). At nodal stations perpendicular to strike (stations S_6 and S_{20}), there is no *SH* arrival in any model. These features arise because the *SH* nodal planes cut through the centre of the focal sphere, passing through parts of the focal sphere that are sampled by seismometers at teleseismic distances. Changes in dip within the source rotate the *SH* focal sphere such that the nodal planes sweep across the region in the lower hemisphere projection covered by the take-off angles of teleseismic waves. This effect makes *SH* waveforms highly sensitive to changes in down-dip curvature. Small changes in curvature therefore have a large effect on the *SH* waveforms at stations within $\sim30°$ of fault strike. Therefore, to detect down-dip curvature in real earthquakes it is essential to include *SH* data from stations in the along-strike directions. This finding is consistent with the observations made by Braunmiller & Nábělek (1996).

The shape of synthetic *P* waveforms is much less sensitive to station azimuth and degree of curvature (Fig. 4), because the *P*-wave nodal planes of normal-faulting earthquakes cut through parts of the focal sphere that are distant from the take-off angles of seismic waves received at stations at teleseismic distances. There are small changes in the width and location of peaks in the waveform, however the main effect is on the amplitude of the waveform, particularly at stations that lie perpendicular to strike. Considering the true (E-dipping) nodal plane that represents our synthetic normal fault, for positive curvature models (convex), stations that lie in the down-dip (East) direction have smaller amplitude and more complex *P* waveforms than stations in the up-dip (West) direction. The opposite is true for negative curvature (listric) models. This effect is stronger for models with greater curvature, as the dip of one subsource is steep and the projection of the relevant nodal plane passes close to stations in the focal sphere, resulting in less energy being received and smaller amplitudes being recorded at those stations (Fig. 5).
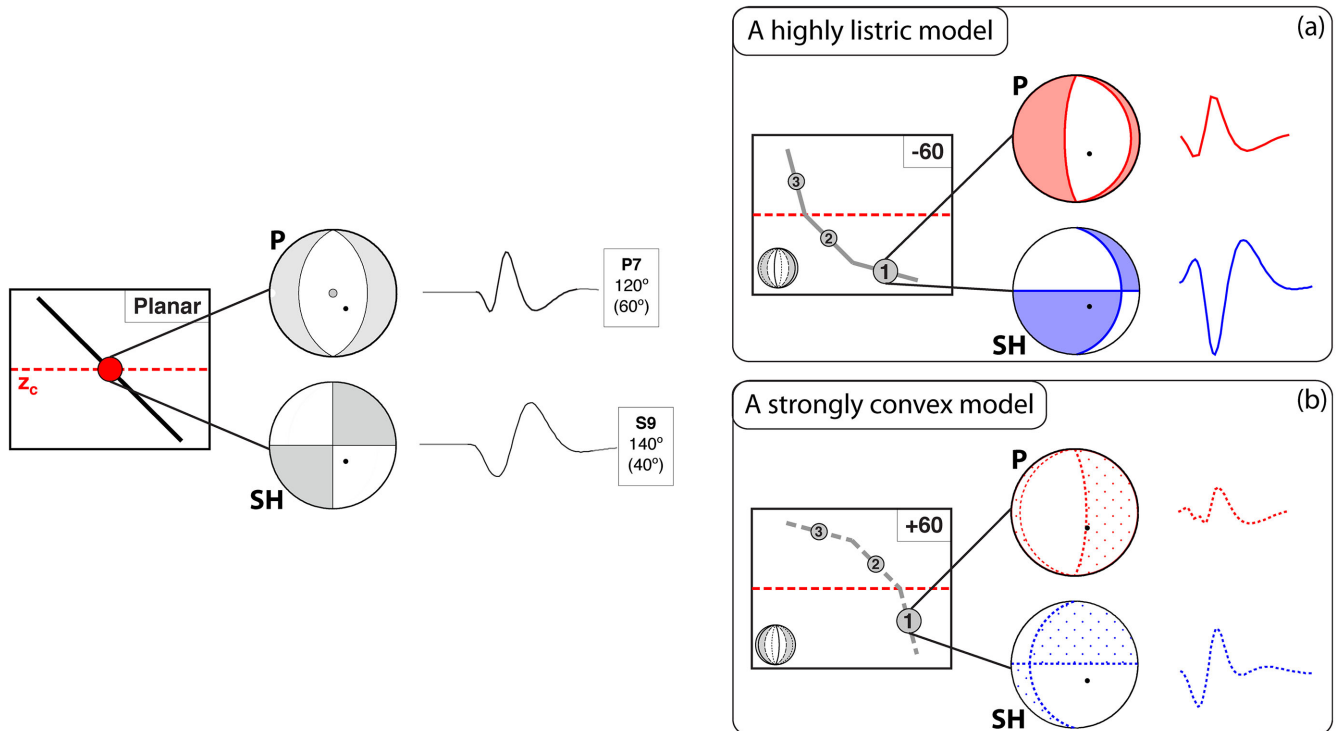
Figure 3. Synthetic *SH* waveforms generated for a M_w 5.9 normal-faulting earthquake, with a strike, average dip and rake of 000°/45°/270°. *SH* waveforms were generated at the synthetic stations shown here, at an epicentral distance of 55°, which is typical of the epicentral distance ranges of teleseismic data used in body waveform inversions. The station position (intersection of the ray path with the lower hemisphere projection of the focal sphere) is shown with a solid black dot on the *SH* focal sphere. Synthetic waveforms are plotted around the *SH* focal sphere (which shows the nodal surfaces for an event with 0° down-dip curvature) at the approximate station azimuth, and labelled with the alphanumeric station name (bold) and azimuth. Synthetic *SH* waveforms, generated from tri-planar models, are shown for events with ±10°, 20°, 40°, 60° and 80° curvature in blue. Solid blue lines are for negative curvature (listric), dotted blue for positive curvature (convex up). Model curvature increases radially outwards, that is, the inner ring shows waveforms for models with 10° curvature, the outer 80°. Synthetics for curved models (blue) are plotted on top of a synthetic single-plane, 1-source centroid model (black) with 0° curvature.

Figure 4. Synthetic *P* waveforms generated for a M_w 5.9 normal-faulting earthquake, with a strike, average dip and rake of $000°/45°/270°$. Key as for Fig. 3, but curved model synthetics are in red and the *P* focal sphere is shown, with compressional quadrants shaded in grey. The *P* stations are at an epicentral distance of $60°$, and the station position (intersection of the ray path with the lower hemisphere projection of the *P* focal sphere) is shown with a solid black dot.

Figure 5. The effect of a high degree of model curvature on synthetic waveforms. This figure illustrates that stations at azimuths >30° from strike may also be sensitive to down-dip curvature. Left: Model fault geometry and *P* and *SH* focal spheres for synthetic single-source planar M_w 5.9 event, as for Fig. 2. Example synthetic waveforms for stations P7 and S9 are shown to the right of the appropriate focal sphere. For both the *P* and *SH* focal spheres, quadrants with positive waveform arrivals are shaded grey, and the appropriate station ray path intersection is marked with a black dot. Station labels are as for Figs 3 and 4. Right: Tri-planar models with 60° down-dip curvature, as for Fig. 2. The synthetic *P* (red) and *SH* (blue) waveforms for stations P7 and S9 are shown to the right; solid line for negative curvature, dotted for positive. The synthetic waveforms are the signal resulting from the summed contribution of the radiated energy from all three subsources, however we show the *P* and *SH* focal spheres for only the first (deepest) subsource, S_1, which affects the initial part of the waveform. The quadrants with positive arrivals from S_1 are shaded and the intersection of the ray path for station P7 and S9 on the focal sphere is shown with a black dot. The dip of S_1 affects the position of the nodal surfaces relative to the station position, and the resultant polarity of the initial part of the waveform.

3.2 Implications for modelling real events

If seismogenic faults have only small degrees of down-dip curvature, the diagnostic signals (*SH* waveform complexity and/or initial low-amplitude peaks with the wrong polarity) will only be detectable at stations lying at positions at or very close to along-strike. Identifying the shapes of the waveforms correctly requires picking the precise onset times for *P* and *SH* arrivals. Stations that lie near an *SH* nodal surface receive a lower energy signal and show lower amplitude *SH* arrivals in seismograms than stations lying elsewhere in the *SH* focal sphere. Along-strike broadband data must be examined carefully for clear arrivals that can be distinguished from the background noise. Picking the wrong *SH* arrival time would skew any attempt to resolve down-dip curvature. For this reason we pick the waveform arrivals by hand, and when modelling real earthquakes we include data from as many along-strike stations as possible, so that one wrong or uncertain *SH* arrival pick will not adversely distort the results.

4 APPLICATION TO REAL EARTHQUAKES

We present a seismological, forward-modelling technique for determining the down-dip geometry of earthquake-generating dip-slip faults, based upon the synthetic models described above. We have applied this method to a catalogue of continental and oceanic events and present the results of the modelling in the next section.

4.1 Event selection

We performed body-waveform inversions for a catalogue of normal-faulting events (Table 1), from a wide range of extensional environments. We then selected suitable earthquakes on which to apply our seismological technique for determining down-dip curvature. Events were chosen based on (1) magnitude, (2) source time function, and (3) station signal-to-noise ratio and distribution. Events need to be large enough ($\geq M_w$ 5.5) that the seismic contributions from different parts of the rupture plane are distinct and separate in space and time; and small enough ($\leq M_w$ 6.5) that the approximation of the earthquakes as a point source (centroid), on which the initial waveform inversion is based, is still valid. Factors such as changes in the rupture propagation direction, uneven moment release, or earthquake doublets, have a large effect on the resultant waveforms recorded at teleseismic distances. This level of complexity leads to multiple trade-offs with down-dip fault geometry. Therefore we select events that are one-segment ruptures, with relatively simple source time functions. In order to perform the modelling effectively there must be a good azimuthal distribution of stations at teleseismic distances, a high density of stations at close to along-strike azimuths, and seismograms with clear arrivals and a high signal-to-noise ratio.

4.2 Procedure

The main stages of the method are as follows:

Table 1. Events used in this study.

Name	Region	Lat (°)	Long (°)	yymmdd	hh:mm:ss	M_w	M_0 (N m)	Strike (°)	Dip (°)	Rake (°)	Depth (km)
L'Aquila	Italy	42.370	13.319	090406	01:32:42	6.2	2.60×10^{18}	134	46	261	4.6
Colfiorito	Italy	43.079	12.781	970926	09:40:27	5.8	6.67×10^{17}	123	40	270	5.4
Aegion	Greece	38.440	22.307	950615	00:15:50	6.2	2.34×10^{18}	290	27	305	11.6
Grevena	Greece	40.143	21.717	950513	08:47:14	6.4	4.39×10^{18}	245	39	271	11.2
Simav	Turkey	39.128	29.070	110519	20:15:25	5.8	7.02×10^{17}	116	37	274	9.5
							7.02×10^{17}	291	53	269	9.5
Palu	Indonesia	−1.085	119.878	090302	00:03:41	5.6	2.82×10^{17}	313	39	273	7.4
							2.82×10^{17}	128	51	265	7.4
MAR	Mid-Atlantic Ridge	26.552	−44.629	070301	23:11:52	5.9	7.84×10^{17}	204	50	289	7
							7.84×10^{17}	024	42	293	7
Gakkel Ridge	Arctic Sea	84.913	99.618	050306	05:21:40	6.2	2.95×10^{18}	133	44	264	9.4
							2.95×10^{18}	315	48	267	9.4
Zhongba 1	Tibet	30.681	83.650	040711	23:08:44	6.2	2.23×10^{18}	163	40	268	10.5
Zhongba 2	Tibet	30.481	83.657	050407	20:04:40	6.2	2.26×10^{18}	165	44	266	7.8
Karonga 1	Malawi	−10.158	33.825	091206	17:36:37	5.7	4.44×10^{17}	164	38	270	4.2
Karonga 2	Malawi	−9.983	33.819	091208	03:08:57	5.8	5.77×10^{17}	146	44	248	5.4
Karonga 3	Malawi	−10.019	33.831	091219	23:19:17	5.9	8.25×10^{17}	158	43	262	5.3

Hypocentre locations and times were retrieved from the ISC; location data for events occurring prior to 2009 is from the EHB bulletin. The centroid parameters were obtained through body waveform inversion in this study. If the true fault plane is not known, parameters for both nodal planes are shown.

(i) Perform a body waveform inversion to obtain point-source centroid focal parameters, moment and source time function for the chosen event.

(ii) Use centroid solution to estimate source dimensions and set up geometry of tri-planar models.

(iii) Generate synthetic waveforms for tri-planar models with a range of down-dip curvatures.

(iv) Compare model synthetics with observed seismograms to constrain down-dip curvature.

4.2.1 Body waveform inversion procedure

Teleseismic data was downloaded using the IRIS (Incorporated Research Institutions for Seismology) Wilber III system and *P* and *SH* arrivals were manually picked on broadband seismograms. A full list of stations we used, along with their network codes, is found in Appendix C in the Supporting Information. We used data from all networks with suitable records, and restrict the station epicentral distance range to 30°–90° and 30°–80° for *P* and *SH* data respectively. This ensures that the *P* and *S* signals are not affected by arrivals of waves that have diffracted, reflected or travelled through the core, and that they have not been affected by shallow lithospheric phases (e.g. Moho head waves). The broadband seismograms are first deconvolved from their instrumental response, and then reconvolved with the response of a long-period (15–100 s) World-Wide Standardized Seismograph Network (WWSSN) instrument. This procedure means that earthquakes of magnitudes M_w 5.0–6.5 can be modelled as a finite-duration rupture at a point source (centroid). We then used the MT5 programme of Zwick *et al.* (1994), based on the algorithm of McCaffrey & Abers (1988) and McCaffrey *et al.* (1991), to jointly invert *P* and *SH* waveforms for earthquake source parameters (strike, dip, rake, centroid depth, moment and source time function). Given an initial model (taken from the GCMT catalogue) and our arrival time picks, we generate synthetic *P* and *SH* waveforms and solve iteratively for the source parameters that give a minimum misfit between the observed waveform and synthetics within the inversion window. The inversion window starts at the picked arrival time and the length is set for

P and *SH* data so that it includes only the body waveforms and their depth phases, and no additional phases. *P*, *pP* and *sP* phases are modelled on vertical component seismograms and *S* and *sS* phases on transverse component seismograms. Synthetics are computed based on the source parameters and calculated take-off angles (with amplitudes corrected for geometrical spreading and attenuation). We solve for the strike, dip and rake of the source (which dominantly affect the shape of the waveforms), and the centroid depth and source time function (which chiefly control the length and amplitude of the waveforms). The source is constrained to be purely double-couple. A full description of this procedure can be found in Taymaz *et al.* (1991) and Nábělek (1984), and similar waveform inversion techniques are used extensively in the literature (Bergman & Solomon 1985; Braunmiller & Nábělek 1996; Craig *et al.* 2011; Sloan *et al.* 2011). This technique refines the accuracy of source parameter estimates made by routine catalogues such as the GCMT, particularly for the centroid depth. The degree to which each focal parameter can be resolved is determined by fixing a parameter, for example, depth, at a series of values away from the best fit, and re-inverting for all other parameters. The fit of the synthetic to the observed seismograms is then compared at successive values of the fixed parameter to determine the range over which a reasonable fit has been found. Typical errors are ±4 km for depth, ±10° for strike, ±5° for dip and ±10° for rake (Molnar & Lyon-Caen 1989; Taymaz *et al.* 1991; Craig *et al.* 2014).

We used a simple crustal velocity model consisting of a half-space of $V_p = 6.5 \, \text{km s}^{-1}$, $V_s = 3.7 \, \text{km s}^{-1}$, $\rho = 2800 \, \text{kg m}^{-3}$. Discrepancies between the model velocity structure and the actual (unknown) velocity profile at the location of each earthquake (e.g. due to shallow, low-velocity sedimentary layers above the source) affect the estimated centroid depth, but not the geometry of the nodal planes (e.g. Bergman & Solomon 1985; Nelson *et al.* 1987; Taymaz *et al.* 1990; Middleton & Copley 2013). The lack of sensitivity of the orientation of the focal planes to the velocity model results from the constraint that the source be comprised of double-couple subsources, and the simultaneous inversion of *P* and *SH* waves at all stations (Fredrich *et al.* 1988).

Table 2. Results from down-dip curvature modelling. Plain grey bars delimit range of down-dip curvature investigated for each event. Grey boxes indicate the extent to which down-dip geometry can be constrained—they show cross-sections of the model geometries that produce synthetics with an acceptable fit to recorded broadband seismograms. The red line marks the modelled centroid depth with respect to the model fault plane. Red dots mark the centroids for the events that show no resolvable evidence for down-dip curvature; orange dots mark the subsource centroids for our preferred tri-planar fault model for events where there is evidence for down-dip curvature. If the true fault plane (FP) is not known, modelling results for both nodal planes are shown (NP1 and NP2).

Event name		Down-dip curvature modelling results															
		−80	−70	−60	−50	−40	−30	−20	−10	0	+10	+20	+30	+40	+50	+60	+70	+80
L'Aquila	FP																	
Colfiorito	FP																	
Aegion	FP																	
Grevena	FP																	
Simav	NP1																	
	NP2																	
Palu	NP1																	
	NP2																	
MAR	NP1																	
	NP2																	
Gakkel Ridge	NP1																	
	NP2																	
Zhongba 1	FP																	
Zhongba 2	FP																	
Karonga 1	FP																	
Karonga 2	FP																	
Karonga 3	FP																	

4.2.2 Constraining down-dip geometry

Having obtained a centroid solution for the earthquakes we study, we use the same procedure as that for the synthetic event (described above) to set up tri-planar models with down-dip curvature (Fig. 1). The MT5 programme (Zwick *et al.* 1994) is used to generate synthetic *P* and *SH* waveforms for the curved tri-planar models at all stations used in the initial inversion. As a first indicator of down-dip curvature in the source, we look for complex *SH* waveform shapes with higher than expected amplitudes at stations within 30° of the along-strike azimuth. We then attempt to put constraints on the down-dip geometry by determining the range of down-dip curvature models that produce an acceptable fit to all the waveform data. For each *SH* station (including those >30° from strike) and for every tri-planar curvature model, synthetic waveforms are compared to the observed seismogram, and the synthetic from the planar solution, in order to determine whether the synthetics produced with a curved fault plane yield a better fit to the observed data, and over what range of curvature there is an acceptable fit to the waveforms.
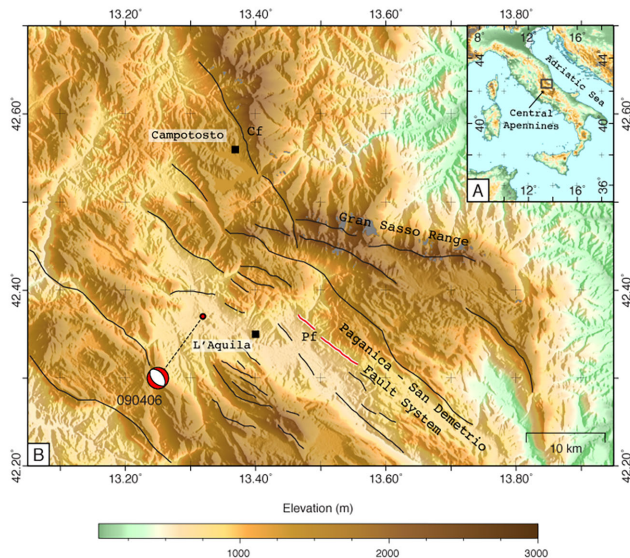
We calculate the variance of the residuals between the recorded signals and the synthetic waveforms within the inversion window, and plot graphs of variance against curvature for *SH*-waveforms recorded at stations within 30° of strike. The important observations are how the misfit varies as a function of curvature for each station. The waveforms are visually inspected to check for features that may skew the plots or produce a misleading variance, such as synthetics

that fit most of the waveform but have the wrong first motion (which would give a low variance of the residuals, despite having the wrong first motion), or the presence of noise in some seismograms (which may result in a high variance, even if the synthetic broadly fits the observed waveform). In order to constrain the down-dip curvature of an event, we examine the visual fit of synthetics together with the graphs of variance against curvature. If down-dip curvature is present, we expect to see a consistent agreement across the *SH* stations, with improved fits at curved models; though we expect the stations >30° from strike to be much less sensitive. Finally, to determine a preferred model, and to avoid biases due to uneven azimuthal distribution of stations or biases in favour of fitting *SH*-waveforms at the expense of *P*-waveforms, we examine the fit of the curved models as a whole, to all *P*- and *SH*-waveforms. Looking for common features among multiple stations is diagnostic of source, rather than receiver, effects.

5 RESULTS

We present the results of body-waveform inversions (Table 1) and the constraints on the down-dip geometry (Table 2) of 13 events. We begin by presenting the source parameters and modelling results for a well-studied event, the 2009 L'Aquila earthquake. There are multiple independent geophysical inversion and aftershock studies for this event, against which we compare the results of our

Figure 6. Map of the Abruzzo Region, central Apennines, Italy (a) Regional map. The perimeter of box B is shown in dark grey. (b) Topography of the 2009 April 6 L'Aquila earthquake epicentral region. The focal mechanism obtained in this study is shown offset from the EHB location. Settlements (black squares) and major features are named. Known and active faults are in black, after Roberts & Michetti (2004); Chiarabba *et al.* (2009); EMERGEO Working Group (2009). The surface trace of the main-shock fault, the Paganica Fault (Pf), is marked in red. Part of the Campotosto Fault (Cf) was activated by an aftershock.

seismological technique, and test that the method is robust. We then describe the constraints on the down-dip geometry for the additional events that we studied; seven in the main text and five others in Appendix D in the Supporting Information.

We first detail the events with no evidence of down-dip curvature and describe to what extent the down-dip geometry can be constrained. We then describe the results for two groups of earthquakes (the Karonga sequence, East Africa, and the Zhongba earthquakes, Tibet) for which there is evidence of down-dip curvature in some events, and present the solution for our preferred model.

For every event, the full solution of the initial body-waveform inversion (planar) and the solution for our preferred model geometry (if different) is in Appendix E in the Supporting Information, modelling of auxiliary planes (if the true fault plane is not known) is presented in in Appendix F in the Supporting Information, and synthetic *P*- and *SH*-waveforms for all models and stations are presented in Appendix G in the Supporting Information.
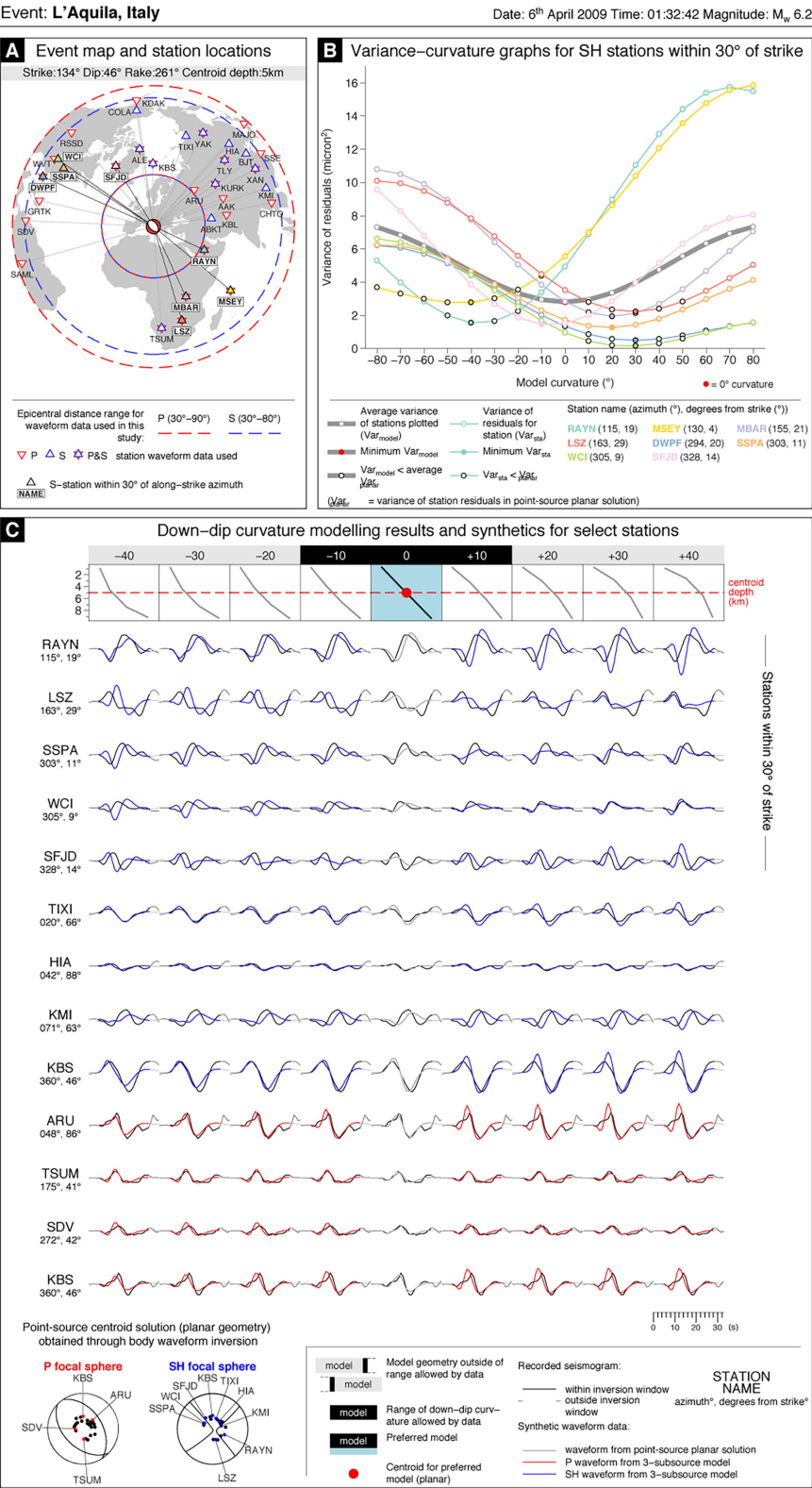
5.1 Test case: the 2009 April 6 L'Aquila earthquake, Italy

The 2009 April 6 M_w 6.2 L'Aquila earthquake ruptured part of an NW–SE-trending fault system (Fig. 6) running through the central Apennines. Body-waveform seismology (e.g. Walters *et al.* 2009; Pondrelli *et al.* 2010; Scognamiglio *et al.* 2010; Herrmann *et al.* 2011), InSAR (e.g. Atzori *et al.* 2009; Walters *et al.* 2009), GPS (Anzidei *et al.* 2009; Cheloni *et al.* 2010; Serpelloni *et al.* 2011), GPS and strong motion (Cirella *et al.* 2009) and aftershock location (Chiarabba *et al.* 2009; Chiaraluce *et al.* 2011; Valoroso *et al.* 2013) studies agree on the first order source parameters (normal motion with a small component of right-lateral slip on a fault striking 127°–144°, dipping 45°–56° to the southwest), which are consistent with the those presented in this study (Fig. 7a).

Geologic mapping and analysis of coseismic surface ruptures (EMERGEO Working Group 2009; Falcucci *et al.* 2009; Boncio *et al.* 2010; Bonini *et al.* 2014), up-dip surface projections of fault plane solutions and analysis of the ground displacements measured by InSAR and GPS (Atzori *et al.* 2009; Walters *et al.* 2009) demonstrate that the main shock ruptured the Paganica Fault. There is some disagreement on whether coseismic slip only occurred up-dip of the 8–10 km hypocentre (Herrmann *et al.* 2011; D'Agostino *et al.* 2012) or whether there was also a deeper slip patch between 9–14 km (Cirella *et al.* 2009; Cheloni *et al.* 2010), however most of the slip was shallower than the hypocentre. Our modelled centroid depth of 5 km, and the depth extent of model fault geometries (1–10 km) are consistent with the estimates of the extent of the fault plane in the source parameter studies mentioned above (1–15 km depth).
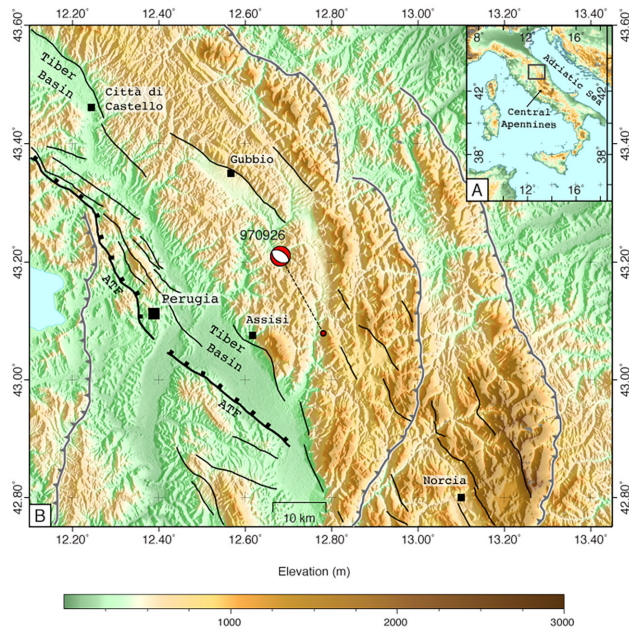
Of eight stations within 30° of strike, six have *SH*-synthetics with a good fit to the observed data for the planar solution (e.g. RAYN, WCI; Fig. 7c). Models with >10° of curvature produce synthetic *SH*-waveforms for which the overall waveform shape and/or peak amplitudes and polarities are significantly different to the observed waveforms at these stations, that is, the recorded data precludes fault geometries of ≥20° of curvature for this event. Recorded waveforms at the other two stations in this azimuth range (MSEY and DWPF) are not fit well by the planar solution synthetics (most likely due to station noise of unknown origin); varying the down-dip geometry does not yield a better fit. Synthetics generated from some curved models yield fits that are equally good or better than the planar case for individual stations (e.g. WCI +30°; Fig. 7c). However, as all the stations record the same event, it is important to find a model that is consistent with the recorded *P* and *SH* waveforms at the majority of stations, rather than a model that yields excellent fits at only some of the along-strike *SH* stations. There is no consistent trend among the stations as a whole favouring either positive or negative curvature, and minor improvements in fit at individual stations are likely due to fitting noise. This feature is demonstrated by the differing minimum-variance model for each of the *SH*-stations within 30° of strike (Fig. 7b). The average variance of the residuals for these stations is lowest for a model with 0° curvature (i.e. planar). *SH*-stations at azimuths >30° from strike have wider ranges of down-dip curvature over which the model produces synthetics with an acceptable fit to the recorded data (e.g. TIXI; Fig. 7c); those that lie roughly perpendicular to strike are insensitive to changes in model geometry (e.g. HIA). Increasing the down-dip curvature produces only small amplitude changes in synthetic *P*-waveforms at most stations (e.g. TSUM), but large changes in stations with high take-off angles and that lie near a *P* nodal plane (e.g. KBS, ARU). For these stations, models with >20° curvature produce synthetic *P*-waveforms with larger amplitudes compared to the other stations (and compared to the planar model). We do not observe this azimuthal variation in the recorded *P*-waveform data. Taken as a whole, all these observations combined mean that we infer that the L'Aquila earthquake ruptured a planar fault. If there is a change in dip in the down-dip direction, it is not more than ±10°.

Chiarabba *et al.* (2009), Chiaraluce *et al.* (2011) and Valoroso *et al.* (2013) relocated large catalogues of foreshocks and aftershocks associated with the L'Aquila main shock. All three studies showed tight clustering of the relocated events along a plane dipping ~50° to the southwest. Their close spatial alignment argues for the Paganica Fault having a planar down-dip geometry, consistent with the results of our analysis of teleseismic body waveforms and down-dip curvature modelling. The corroboration of our result by other geophysical methods demonstrates the robustness of the technique.

Figure 7. Down-dip curvature modelling results for the 2009 April 6 L'Aquila earthquake.Figure overleaf. (a) Event location map, focal mechanism and distribution of stations. Centroid parameters obtained through body waveform inversion (planar solution) are shown above the map; the focal mechanism is plotted at the location of the epicentre. Stations used in the inversion are named. (b) Plots of variance against curvature for *SH*-stations within 30° of strike. Variance was calculated for the residuals between synthetic and recorded *SH*-waveforms, within the inversion window used to obtain the initial centroid solution, for each station and tri-planar model. (c) Down-dip curvature modelling results and synthetics for select stations. Cross-sections through model fault geometry are shown above. The range of curvature constrained by the data is highlighted in black, the best-fit model geometry in blue. Synthetic waveforms calculated for three-subsource models for select stations are plotted below (red for *P*-, blue for *SH*-waveforms), on top of the recorded waveform (black). For the 0°-curvature model, the synthetic from the point-source planar solution (grey) is plotted on top of the recorded waveform. The station positions are shown on the relevant focal sphere.

Figure 8. Map of the Umbria-Marche Region, central Apennines, Italy.(a) Regional map. The perimeter of box B is shown in grey. (b) Topography of the 1997 September 26 Colfiorito earthquake epicentral region, overlaid with a simplified fault map (after Chiaraluce 2003). Settlements (black squares) and major features are named. Pre-exisiting, inactive thrusts are in grey, SW-dipping normal faults in black, and the trace of the major NE-dipping, Alto-Tiberino normal fault (ATF) is bold. The focal mechanism obtained in this study is shown offset from the EHB location.

Based on modelling of regional broadband waveforms and extensive finite-fault models of velocity and accelerometer data, Herrmann *et al.* (2011) concluded that the major moment release in the L'Aquila earthquake occurred up-dip of and, 4–7 s after, the rupture initiation at the hypocentre. Cirella *et al.* (2009) jointly invert strong motion and GPS data and find that slip propagated up-dip with a velocity of 2.2–2.8 km s^{-1}. These independent analyses further support our model assumptions; an upwards-propagating rupture, and the choice of a 2.5 km s^{-1} rupture velocity.

5.2 Planar ruptures

Our analysis shows that the majority of normal-faulting earthquakes that are large enough to rupture through the seismogenic layer occur on planar faults. These events showed no strong evidence for down-dip curvature, had dips between 30°–60°, and could be constrained to be planar to within ±20°. We describe in detail below the 1997 September 26 Colfiorito earthquake, Italy, and the 1995 May 13 Grevena earthquake, northern Greece. A full description of our results for the additional planar ruptures (1995 June 15 Aegion earthquake, Greece; 2011 May 19 Simav earthquake, Turkey; 2009 March 2 Palu earthquake, Indonesia; 2007 March 1 earthquake, Mid-Atlantic Ridge; 2005 March 6 earthquake, Gakkel Ridge, Arctic Sea) is presented in Appendix D in the Supporting Information.

5.2.1 The 1997 September 26 Colfiorito earthquake, Italy

The 1997 September 26 Colfiorito earthquake was largest of six $5 < M_w < 6$ events that struck the Abruzzo region (Fig. 8) of central Italy during September–October 1997, known as the Umbria-Marche sequence (Chiaraluce 2003). Our modelled centroid dip

(40°) agrees well with that obtained by other authors through waveform inversion (Ekström *et al.* 1998; Morelli *et al.* 2000), the alignment of relocated aftershocks (Amato *et al.* 1998; Deschamps *et al.* 2000; Chiaraluce 2003) and various geodetic analyses (Hunstad *et al.* 1999; Stramondo *et al.* 1999; Salvi *et al.* 2000; De Martini *et al.* 2003). We obtain a centroid depth of 5 km, consistent with the 4–5.5 km depth of maximum slip obtained by Lundgren & Stramondo (2002) through joint inversion of GPS and InSAR data, and infer the depth extent of faulting to extend between >1 km to <8 km. This depth distribution is supported by observations that very little slip reached the surface (Cinti *et al.* 1999; Cello *et al.* 2000; Basili & Meghraoui 2001), aftershock hypocentres delineate a cut-off in seismicity beneath 8–9 km depth (Deschamps *et al.* 2000; Chiaraluce 2003), and forward-modelling of coseismic displacements on a fault plane with a similar depth extent adequately reproduces measured GPS and InSAR surface displacements (Hunstad *et al.* 1999; Salvi *et al.* 2000).

Our planar solution yields synthetics with moderately good fits to the shape and amplitude of *SH*-waveforms recorded at all stations within 30° of strike (Fig. 9c). Models with ≥20° of curvature produce complex synthetic *SH*-waveforms that do not fit the observed data at these 6 stations, particularly for stations lying SE of the event (e.g. MSEY; Figs 9a and c). The average variance of *SH*-stations within 30° of strike is lowest for models with 0° to +10° curvature (Fig. 9b). For stations >30° from strike, the *SH*-waveforms are less sensitive to changes in the down-dip geometry (e.g. ALE; Fig. 9c), and individual stations have a wider range of curvatures over which the model generates a synthetic that fits the recorded waveform equally well. In general, increasing down-dip curvature has only a small effect on the amplitude of *P*-waveforms (e.g. FURI, FFC; Fig. 9c). Stations with high take-off angles and that lie near a *P* nodal plane (e.g. KBS, ARU; Fig. 9c) exclude geometries with ≥30° of curvature; for these geometries the initial dip is high or low enough that the *P*-synthetic produced at these stations may have the wrong initial polarity and/or a substantially different amplitude compared to *P*-synthetics for other stations and the observed data. There is no evidence to suspect down-dip curvature for this event. The data allows for a maximum of ±10° curvature; outside of this range the fit of synthetics at key stations deteriorates. We therefore infer that the Colfiorito event ruptured a planar fault, to within −10°/+10° degrees.

Some workers have described the faults in the Colfiorito area as having listric geometries (Boncio & Lavecchia 2000; Barchi & Mirabella 2009), because the coseismic faults do not project to the surface while maintaining their 35–45° dips, and exposed fault planes have measured dips of ∼60–70° (Cello *et al.* 2000; Chiaraluce *et al.* 2005). Additionally, it has been suggested that the normal faults bottom-out below ∼8 km, either onto pre-existing, low-angle structures (e.g. the Alto-Tiberino Fault; Boncio & Lavecchia 2000) or into horizons of Triassic evaporites (Mirabella *et al.* 2008; Barchi & Mirabella 2009), though there is a dearth of good quality seismic reflection data to test these suggestions (Chiaraluce *et al.* 2005; Mirabella *et al.* 2008). Although co-seismic displacements do seem to be taken up on high-angle fault strands at the surface—evinced by diffuse aftershock seismicity in the upper 1 km (Chiaraluce *et al.* 2004), complex patterns of surface deformation (e.g. Stramondo *et al.* 1999; Cello *et al.* 2000; Salvi *et al.* 2000; Vittori *et al.* 2000) and reconstruction of levelling-line displacements (Basili & Meghraoui 2001)—modelling of surface displacements indicates that the high-angle structures accommodating this slip only extend to ∼500 m beneath the surface (Basili & Meghraoui 2001). Therefore the faults activated in the
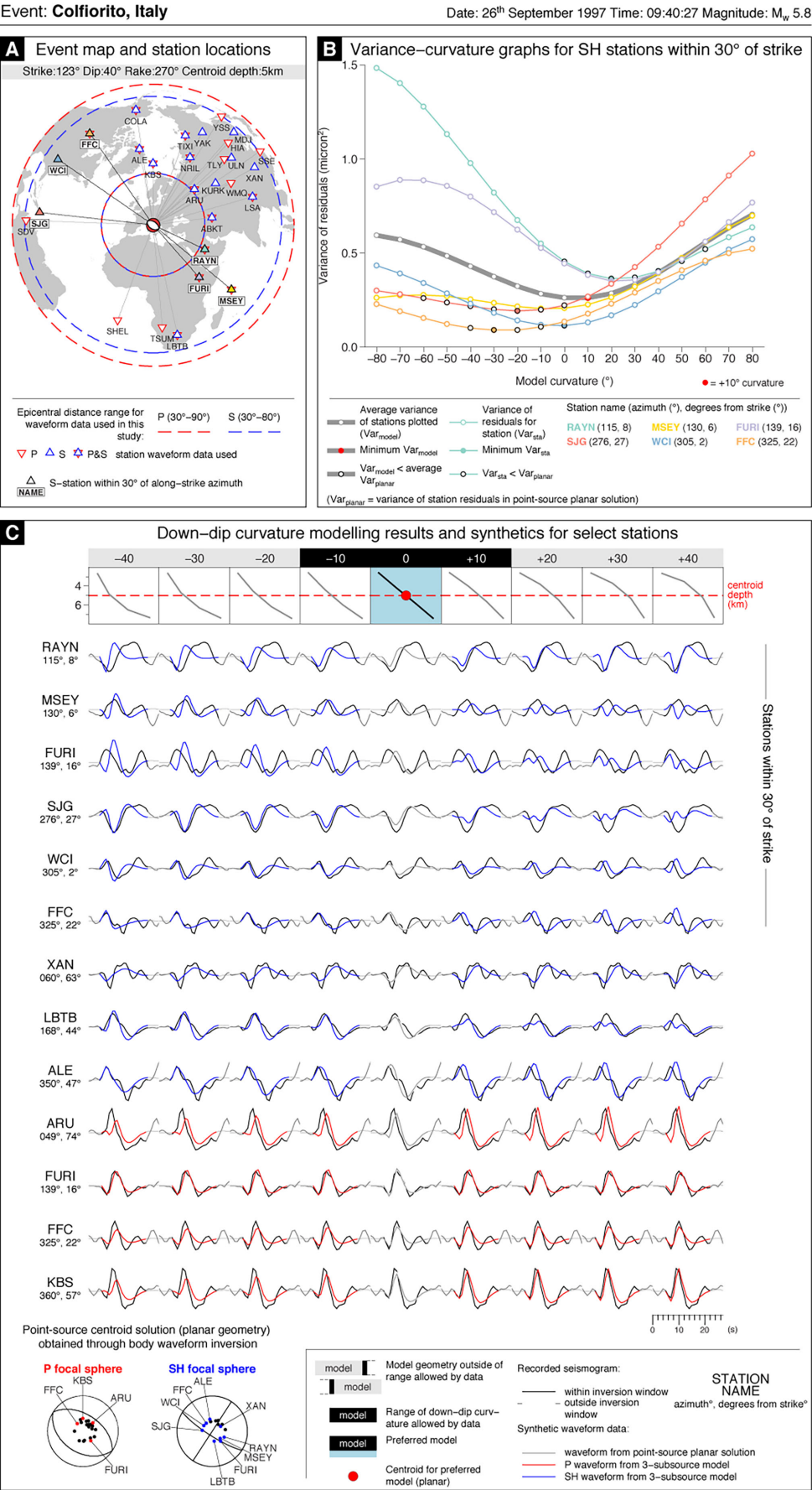
Figure 9. Down-dip curvature modelling results for 1997 September 26 Colfiorito earthquake. Caption as for Fig. 7.
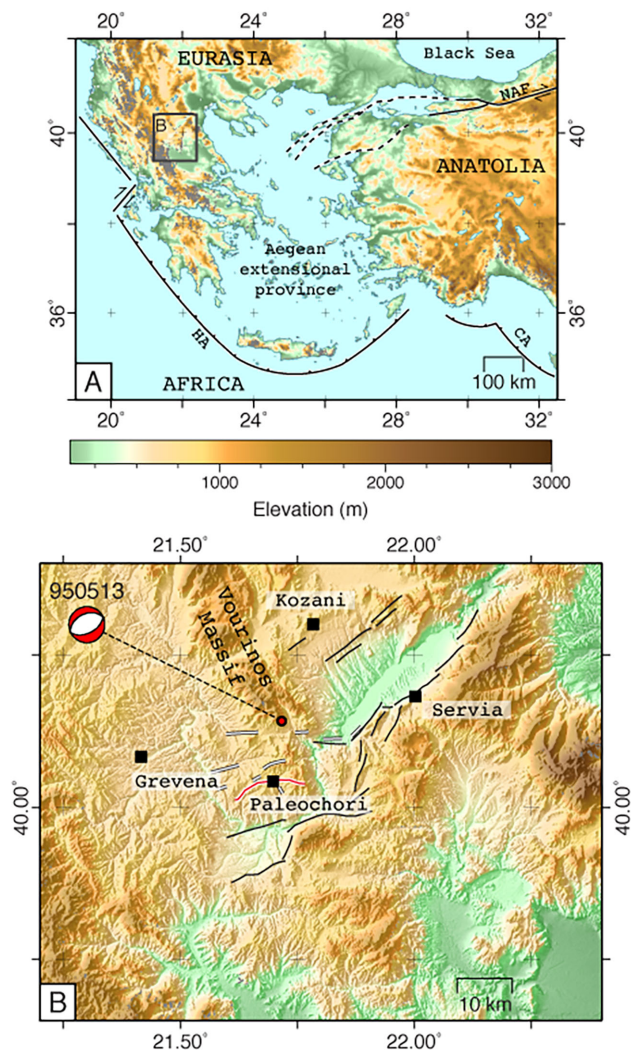
Umbria-Marche sequence are not listric in the sense of a smooth decrease in dip with depth. Instead, the analysis presented here, and the close alignment of aftershock hypocentres, indicates that the faults are planar at the depths where they rupture in earthquakes (Amato *et al.* 1998; Chiaraluce 2003), that is, there is less than ±10° change in dip with depth between ∼2–8 km. The hypocentres of the larger events in the sequence, including the 1997 September 26 event modelled here, are located at depths close to the base of these aftershock clusters (Stramondo *et al.* 1999; Barba & Basili 2000), at the same depth as foreshock activity (Cattaneo *et al.* 2000), and close to the inferred intersection with pre-existing low-angle faults (Chiaraluce *et al.* 2005; Mirabella *et al.* 2008). A lack of seismicity at depths >8 km suggest this decollement, if it exists, is not seismically active. Both the modelling in this study and detailed studies by other workers establish that extension in the seismogenic layer is accommodated by rupture on planar faults in the Colfiorito region.

5.3 The 1995 May 13 Grevena earthquake, Greece

On the 1995 May 13, a destructive M_w 6.4 normal-faulting earthquake hit northern Greece, approximately equidistant from the towns of Grevena and Kozani (Fig. 10). We obtained centroid source parameters consistent with other estimates from body waveform seismology (Hatzfeld *et al.* 1998), inversion of horizontal GPS displacements (Clarke *et al.* 1997) and InSAR studies (Resor *et al.* 2005) to within 10°, and the strike is similar to that measured for the only mapped fault with conspicuous surface rupture (the 250°-striking Paleochori Fault; Meyer *et al.* 1996). We obtained the same centroid depth (11 km) as Hatzfeld *et al.* (1998), and our estimated depth extent of the rupture (6–15 km) is consistent with their 14.2 km main-shock hypocentre and the distribution of aftershocks between 5–15 km.

The planar solution from the body-waveform inversion generates synthetics that fit the shape and amplitude of *SH*-waveforms very well at 11 of 12 *SH*-stations within 30° of strike. There is therefore no indication that there may be down-dip curvature. Models with positive curvature produce complex *SH*-synthetics at these stations which have very different waveform shapes and/or the wrong initial polarity when compared with the observed waveforms (e.g. AAK; Fig. 11c)—this precludes any positive down-dip curvature. Models with negative curvature produce synthetic *SH*-waveforms with similar shapes to the recorded waveforms. Increasing the degree of negative curvature mainly affects the amplitudes, not the shape, of the synthetic waveforms, and yields a better fit of the resultant synthetic to the data for some stations (e.g. KURK −30°). However, for *SH* stations at azimuths 30°–65° from strike, models with more than −20° curvature generate synthetics with amplitudes much larger than the recorded data (e.g. SJG −40°). Synthetics for *SH* stations at azimuths >65° from strike have poor fits irrespectively of model fault geometry, as they lie close to an *SH* nodal surface and so have a poor signal-to-noise ratio. Stations with high take-off angles and lying roughly perpendicular to strike plot near one of the *P* nodal planes in a lower hemisphere projection. Small increases in negative curvature produce synthetic *P*-waveforms with the wrong initial polarity at these stations (e.g. NAI, ATD), ruling out more than −20° down-dip curvature. Plots of variance against curvature are skewed towards negative-curvature models (Fig. 11b), reflecting the extremely high misfits for positive-curvature models. Overall, both *P* and *SH* waveform data support a planar geometry and the down-dip curvature can be constrained to between −20° and 0°.

Figure 10. Map of Northern Greece.(a) Simplified tectonic setting. Major plate-bounding faults in black: NAF, North Anatolian Fault; HA, Hellenic Arc; CA, Cyprus Arc. The perimeter of box B is shown in grey. (b) Local topography map. The focal mechanism obtained for the 1995 May 13 Grevena earthquake in this study is shown offset from the EHB location. Settlements (black squares) and tectonic features are named in black. Simplified active faults, retraced after Resor *et al.* (2005), are delineated in black; location of surface fissures and ruptures mapped by Meyer *et al.* (1996) are in white; the trace of the major surface rupture, the Paleochori Fault (PF) is shown in red.

Most published inversions suggest that the maximum slip and majority of the moment-release occurred on the deeper parts of a fault plane with parameters consistent with the focal mechanisms obtained using body waveform data (e.g. Meyer *et al.* 1996; Clarke *et al.* 1997; Rigo *et al.* 2004; Resor *et al.* 2005). It is therefore not surprising that the best-fit model from the teleseismic waveform modelling in this study is planar. The ability of the forward models to detect down-dip curvature is limited to the parts of the coseismic fault plane that produce a significant contribution to the overall moment. Therefore we do not expect to resolve the up-dip rupture propagation onto high-angle surface-breaking fault strands (if they exist) if they did not produce large offsets. It is likely that the deep main-shock fault connects in some way with the steeper exposed fault planes mapped at the surface, but the nature and geometry of this linkage is unclear. The availability of many different and detailed geologic, geodetic and seismological data sets has allowed
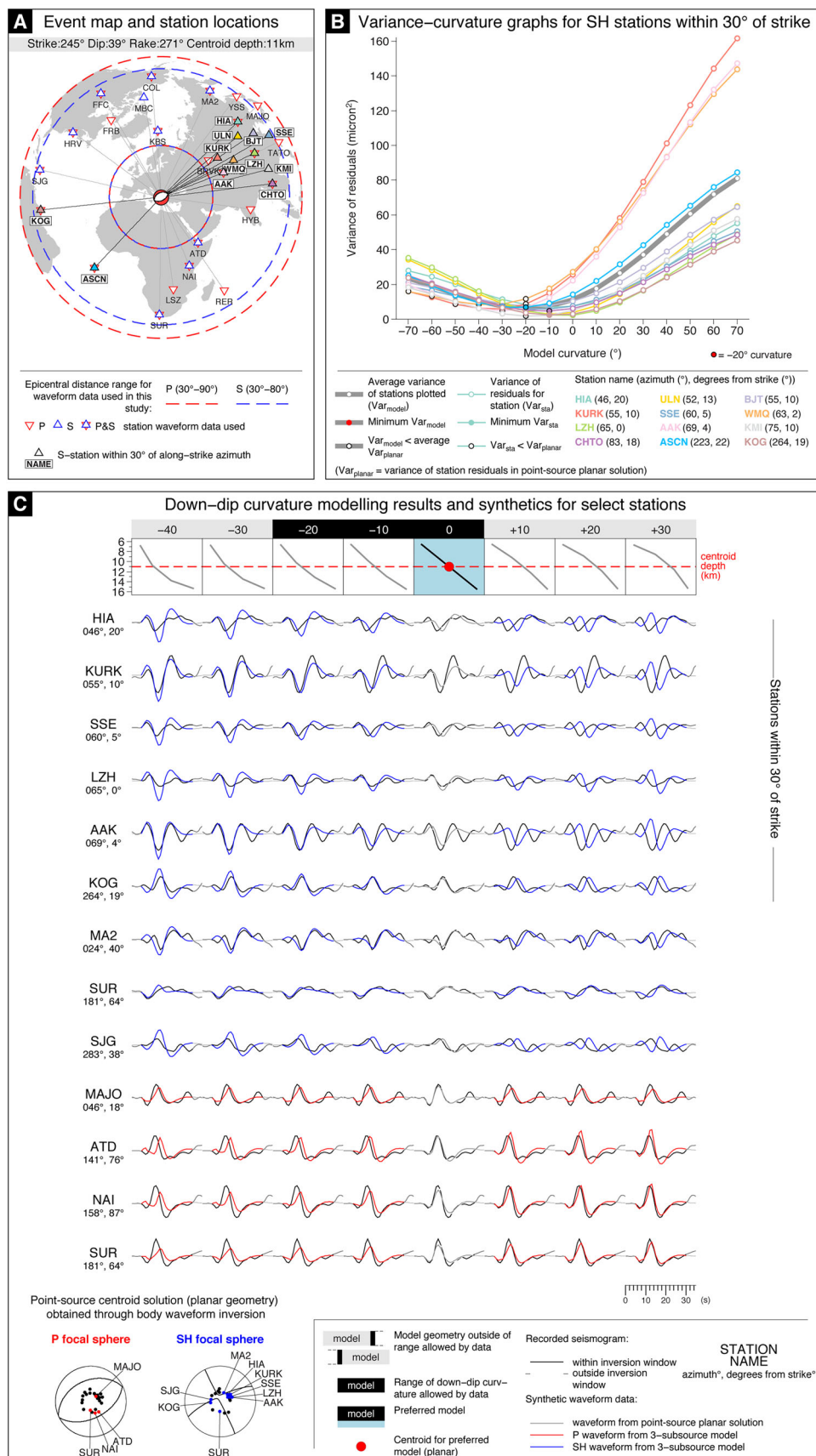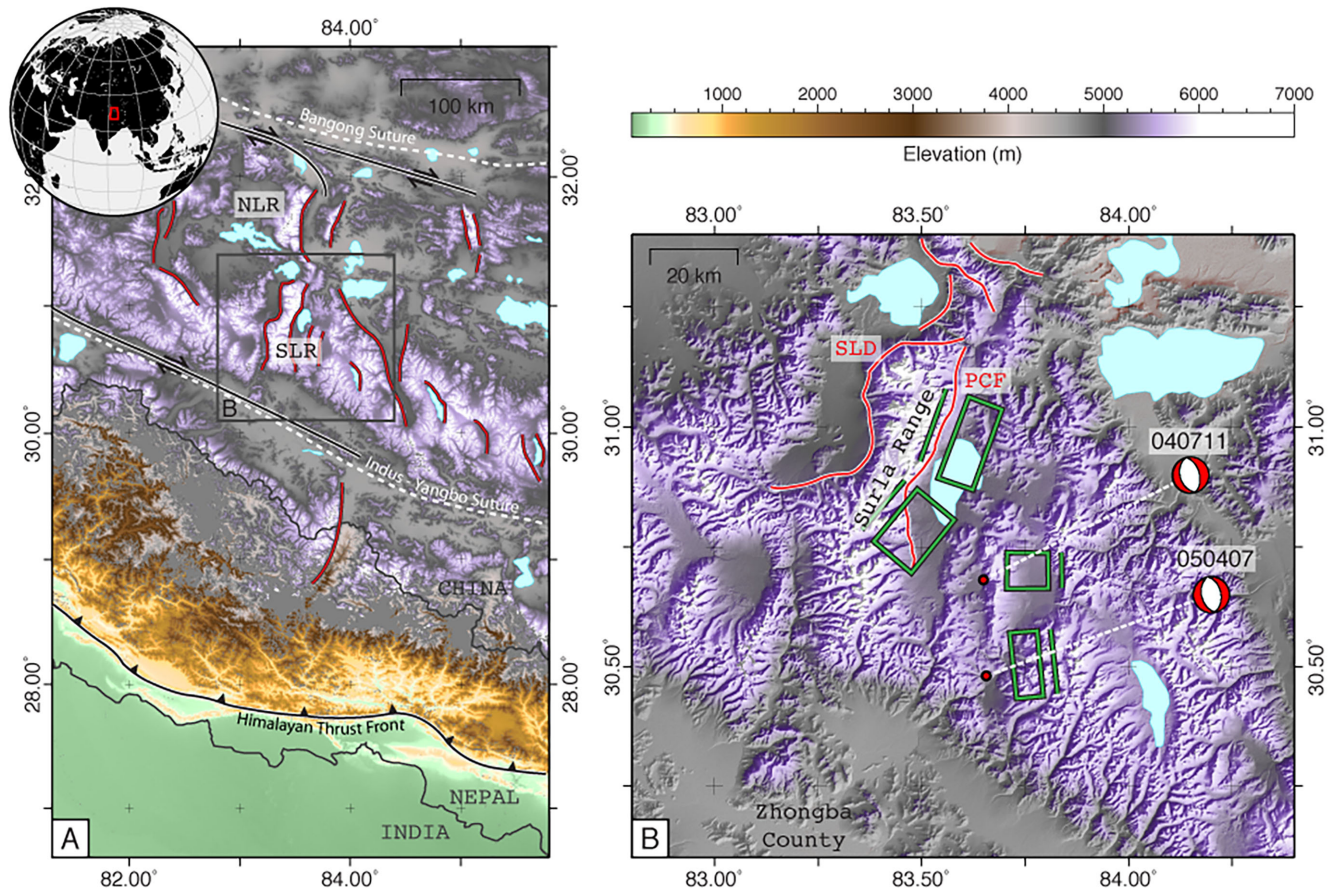
Figure 11. Down-dip curvature modelling results for 1995 May 31 Grevena earthquake. Caption as for Fig. 7.

Figure 12. Map of southwest Tibet. (a) Regional map and simplified structure. Major normal faults in red, strike-slip faults in black and suture zones dashed in white. NLR, North Lunggar Rift; SLR, South Lunggar Rift. Country boundaries are in grey, as is the perimeter of box B. The inset globe shows the location of box A in red. SRTM topography is coloured according to the scale on the right. (b) Topography and structure of the South Lunggar Rift. Focal mechanisms obtained in this study are offset from their EHB locations (red dot) and labelled with a date (yymmdd) identifier. Faults in red, after Styron *et al.* (2013). Outline of model fault planes and up-dip surface projections (green) from the uniform-slip InSAR models of Elliott *et al.* (2010) for the 2004 and 2005 events, and the 2008 doublet.

several studies (e.g. Meyer *et al.* 1996; Resor *et al.* 2005) to build up a detailed picture of the fault network in the Kozani–Grevena region, and given the large moment-release it is not surprising that multiple fault strands, particularly those up-dip and in the hanging wall of the main shock, were activated by the Grevena earthquake. Despite the fine-scale complexity of the fault system, the results of the down-dip curvature modelling in this study suggest that the major coseismic displacements are consistent with rupture on a planar structure.

5.4 Ruptures with down-dip curvature

Based on the analysis of the *SH* waveforms at stations within 30° of strike, there is a strong indication of down-dip curvature in 4 events. Two events (a M_w 5.7 and a M_w 5.8) were from an earthquake sequence that occurred on the Karonga Fault system, Lake Malawi, and which culminated in a M_w 5.9 (included here for completeness, but which does not show any evidence of down-dip curvature). The other two were 2004 and 2005 M_w 6.2 events that occurred in the Lunggar Rift region, Tibet.

5.4.1 The 2004 and 2005 Zhongba events, Lunggar Rift, Tibet

We studied two M_w 6.2 normal-faulting events that occurred in Zhongba county in the Xizang region of southwestern Tibet, China

(Fig. 12). Just north of the Indus suture the tectonics of southern Tibet are characterized by extension across N–S-trending grabens (Armijo *et al.* 1986). The 2004 July 11 and 2005 April 7 earthquakes described here were located in one of these active grabens, the South Lunggar Rift.

The South Lunggar Rift is comprised of a ∼50 km wide central horst, the Surla Range, bounded on either side by the gentle west-dipping South Lunggar Detachment and steeper east-dipping Palung Co Fault (Styron *et al.* 2013). Small fault scarps are observed to cut glacial moraines along the northern portion of the Palung Co Fault (Styron *et al.* 2013), and the up-dip projections of InSAR-modelled fault planes for a 2008 normal-faulting doublet (Elliott *et al.* 2010) also coincide with the range front and mapped fault trace in the north, indicating that the fault is currently active. Elliott *et al.* (2010) performed a study of a series of large normal-faulting events in Tibet, including the two we model here, using InSAR and body waveform seismology. For both events, the surface deformation in InSAR interferograms was best fit by west-dipping faults located east of the Palung Co Fault (Elliott *et al.* 2010, and Fig. 12). The seismogenic thickness is ∼15 km in Tibet (Craig *et al.* 2012), and the magnitude and depth of the earthquakes suggest that they ruptured through most of the seismogenic crust. These two events seem to represent break-up of the hanging wall of the major basin-bounding Palung Co fault on antithetic faults.

2004 July 11 event. Synthetics from the planar solution obtained through body-waveform inversion fit *SH*-waveform data quite well at the nine stations within 30° of strike. However for the majority of these stations, the synthetics are consistently of a lower amplitude than the recorded signal, and do not match the fine detail of the waveform shape (the polarity of the small peaks in the initial part of the waveform) (e.g. OBN, ARU, SFJ; Fig. 13c). These small initial waveform peaks are a strong indication of down-dip curvature. Model geometries with some negative curvature (between −10° to −30°) consistently yield synthetics with better fits to the recorded waveform than for a planar model, particularly with respect to these details of *SH*-waveform shape and amplitude (e.g. ARU −20°, SFJ −30°). This improvement in fit is also reflected in the variance-curvature graphs for stations within 30° of strike (Fig. 13b); eight have minimum variances for models with negative curvature, and the average model variance is lowest for a model with −20° down-dip curvature.

The shape and amplitude of *SH*-waveforms at all stations at azimuths >30° and <55° from strike are also better fit by synthetics from models with −10° to −30° curvature (e.g. MA2 −30°, GNI −20°; Fig. 13c). Stations at azimuths >55° from strike have complex, low-amplitude signals that are not well matched by any synthetics, due to the poor signal-to-noise ratio resulting from their being close to an *SH* nodal plane. From the synthetic modelling presented in Section 3, stations in this azimuth range are not expected to be sensitive to down-dip curvature. Models with any positive down-dip curvature produce synthetic *SH*-waveforms with complex wave shapes and initial peaks with the opposite polarity to the recorded signal at all stations within 47° of strike, ruling out any convex down-dip geometry for this event. For stations that plot near the E-dipping nodal plane in a lower hemisphere projection, models with −40° down-dip curvature or more produce synthetic *P*-waveforms with the wrong initial polarity (e.g. SSE, DAV; Fig. 13c). There is a good overall fit of both *P* and *SH* waveforms at models with −30° to 0° curvature. The results suggest that this event involves down-dip curvature, and the best-fit model is slightly listric, with −20° curvature.

2005 April 7 event. Synthetic *SH*-waveforms generated at five of six stations within 30° of strike for a model with planar down-dip geometry have much smaller amplitudes and different shapes compared to the recorded waveforms (e.g. KONO, KEV; Fig. 14c). Similar to the 2004 event, this is a strong indication of down-dip curvature. Synthetics generated from models with −30° to −10° negative down-dip curvature have very good fits to the data at these stations, in terms of the amplitude, overall shape and polarity of small initial peaks in the waveform (e.g. MBWA −30°, ARU −20°). The fit of the synthetics is significantly better for this range of negative-curvature models than for a planar model geometry. This feature is reflected in the shape of the graphs of variance against curvature for these stations, which have residual variances that tend to a minimum in this model range, and are lower than the variance for the planar model for 4 stations (Fig. 14b). In almost all cases the fit of synthetic *SH*-waveforms to the seismograms is very poor for all models with positive curvature. For strongly listric models (−40° down-dip curvature or more) synthetic *SH*-waveforms have very high amplitudes compared to the recorded waveforms, and the fit of the synthetic deteriorates with increasing negative curvature. The fit of synthetic *P*-waveforms at stations with high take-off angles and at azimuths that are roughly perpendicular to strike (e.g. MAJO, TATO) also becomes significantly worse in this range, as the synthetic waveform has the wrong initial polarity. For almost all stations at azimuths >30° and <50° from strike, models with

−30° to −10° curvature also yield synthetics with a better fit to the recorded *SH*-waveform than synthetics from the planar model, in terms of both the detail of waveform shape and the amplitude of the peak. Based on the analysis of the *SH* waveforms, there is strong evidence for down-dip curvature in the range −10° to −30°. The best-fit model has −20° curvature.

5.4.2 The 2009 Karonga sequence, Lake Malawi

We studied the three largest events (6th December M_w 5.7, 8th December M_w 5.8, and 19th December M_w 5.9) in an earthquake sequence that struck the Karonga region of northern Malawi, on the western shore of Lake Malawi, between November and December 2009 (Fig. 15). The rift basin is strongly asymmetric; the footwall of a steep west-dipping fault (the Livingstone Fault) forms a 2 km high escarpment on the eastern bank of the lake, and its hanging wall is broken up by minor west-dipping faults, mapped by offshore seismic reflection profiles (Flannery & Rosendahl 2009; Ebinger *et al.* 1999). The east-dipping Karonga Fault forms the western-most boundary of the basin and divides the hilly topography and exposures of Precambrian to lower Palaeozoic basement rocks in the west from the flat alluvial plain in the east (Hamiel *et al.* 2012). Following the earthquake sequence, surface breaks were observed in an area north of Karonga city with no previous evidence of surface-rupturing faults, offsetting Quaternary sediments in the flat plain (Hamiel *et al.* 2012; Macheyeki *et al.* 2015). Biggs *et al.* (2010) used seismology and InSAR to demonstrate that the sequence occurred on shallow, west-dipping structures in the hanging wall of the Karonga Fault. It has been suggested that failure initiated on a favourably orientated pre-existing structure, and then migrated to adjacent planes of weakness as a result of static stress transfer (Fagereng 2013).

2009 December 19 event. Unlike the other earthquakes we modelled from this sequence (6th December M_w 5.7 and 8th December M_w 5.8 events), there was no evidence of down-dip curvature for this event. Of nine stations within 30° of strike, the planar solution from the body-waveform inversion generates synthetics with good fits to the shape and amplitude of *SH*-waveforms at five stations (e.g. MAW, TUE, KIEV; Fig. 16c). At the other four, the synthetic wave shape has a poorer fit and the amplitude is lower than the recorded data (e.g. TAM, BFO). Down-dip curvature modelling does yield synthetics with better fits than the planar model, for these stations. However, it also results in *SH*-synthetics with increasingly worse fits to the waveform data for the five stations that are well-matched by the initial planar solution. Positive-curvature models generate very different synthetic *SH* wave shapes, which in some cases have the wrong initial polarity compared to the recorded data (e.g. BFO +20°). Models with negative curvature produce synthetic *SH*-waveforms with high amplitudes, which yield individual best-fit models for some stations (e.g. BFO −30°), but very poor fits for others (e.g. MAW −30°, DPC −30°). The minimum-variance model for most of the ∼along-strike *SH*-stations is between −10° to +10° (Fig. 16b). The average is −10°, however this is most likely skewed by the result for EIL, for which the observed waveform data is not fit well by any model, irrespective of geometry, presumably due to noise in the data.

SH-waveforms at stations at azimuths >30° from strike are less sensitive to down-dip curvature and are overall well-matched by the initial planar solution. Increasing degrees of down-dip curvature generates synthetics with poorer fits (e.g. XMIS, UOSS; Fig. 16c). The complexity, polarities and reduced amplitudes of synthetic
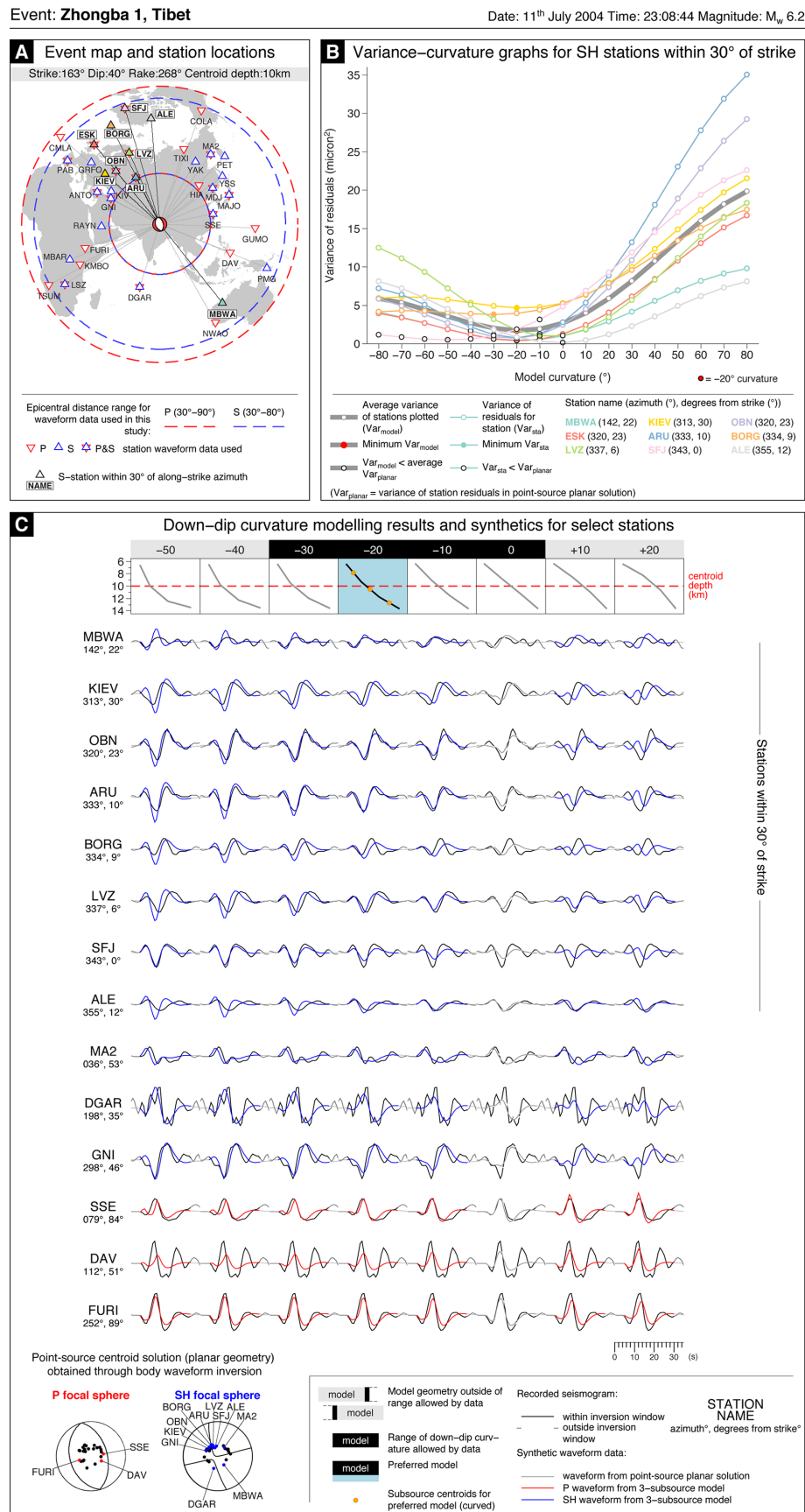
Figure 13. Down-dip curvature modelling results for the 2004 July 11 Zhongba earthquake. Caption as for Fig. 7.
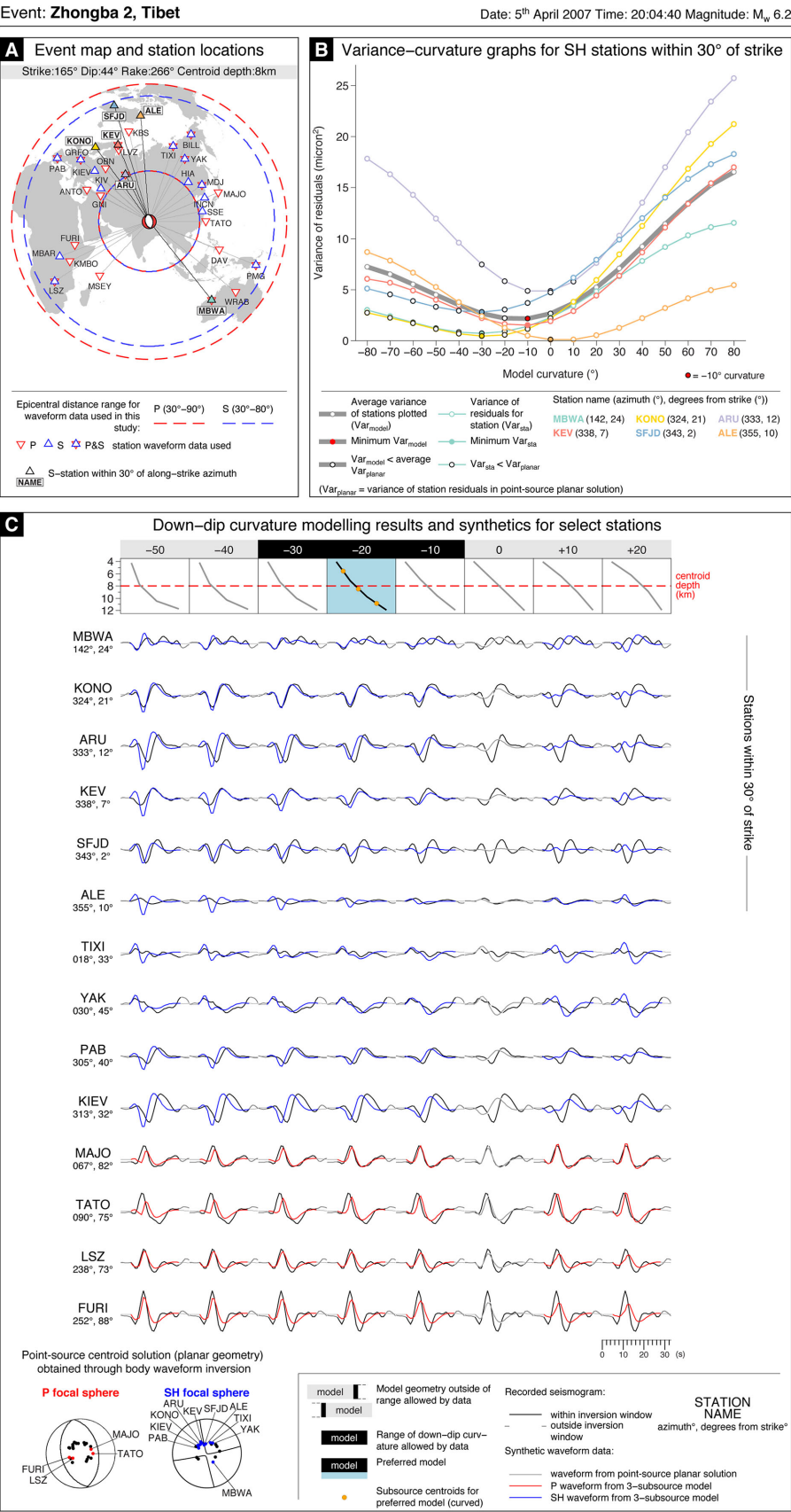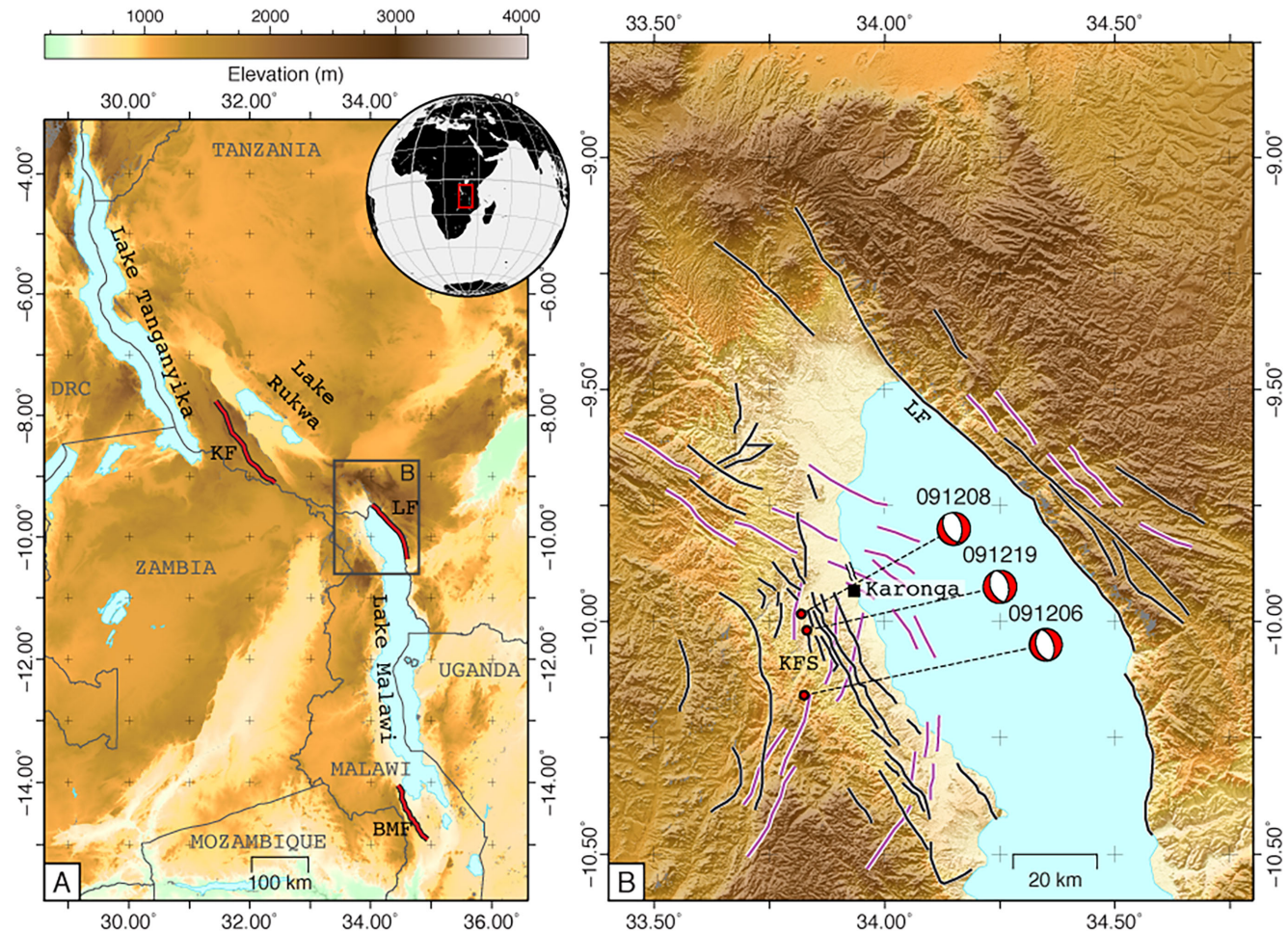
Figure 14. Down-dip curvature modelling results for the 2005 April 07 Zhongba earthquake. Caption as for Fig. 7.

Figure 15. Map of northern Lake Malawi.(a) Regional map of the southern part of the Western Branch of the East African Rift. Country boundaries are in grey, major normal faults mentioned in the text are in red. The traces of the Kanda (KF), Livingstone (LF) and Bilila-Mtakataka (BMF) Faults are after Versfelt & Rosendahl (1989), Jackson & Blenkinsop (1997) and Vittori *et al.* (1997), respectively. The perimeter of box B is shown in grey and the inset globe shows the location of box A in red. (b) SRTM30 topography of northern Lake Malawi (scale to top left). Focal mechanisms obtained in this study are offset from their EHB locations (red dot) and labelled with a date (yymmdd) identifier. The location of Karonga is marked with a black square; KFS is the Karonga Fault system. Faults, delineated in black, are retraced from Biggs *et al.* (2010); the surface ruptures of Macheyeki *et al.* (2015) are in white with a black outline (just N of Karonga). The trend of basement foliations are marked in purple, after Versfelt & Rosendahl (1989)

P-waveforms at stations with high take-off angles and that lie at high angles from strike precludes geometries with >30° down-dip curvature (e.g. KAPI, RCBR). The overall fit of synthetic *SH*-waveforms is significantly worse outside the range −30° to +10°. We therefore suggest that this event in the Karonga sequence ruptured a planar fault.

2009 December 8 event. The planar solution from the body-waveform inversion generates synthetics with similar waveform shapes, but much smaller amplitudes than the recorded *SH*-waveform at all five stations within 30° of strike (e.g. TUE, IDI; Fig. 17c). This is a strong indication of down-dip curvature. Synthetics generated from models with negative down-dip curvature have excellent fits to the data at these stations, both for the waveform amplitude and shape, particularly in the −30° to −60° range. The fit of the synthetics is significantly better for this range of negative-curvature models than for a planar model geometry. This is reflected in the shape of the graphs of variance against curvature for these stations (Fig. 17b). For all five stations, models with negative down-dip curvature yield lower variances than that for the single-plane solution and their respective minimum variances lie in the range −50° to −20°.

For stations at azimuths >30° from strike, there is a wide range of model geometries over which the fit of the synthetic (in terms of waveform shape and amplitude) to the observed *SH*-waveform is adequate. In general the fit is equally good or slightly better for negative-curvature models (e.g. SYO −30°; Fig. 17c), and equally good or slightly worse for positive-curvature models (e.g. SYO +10°). Although the overall fit of *SH*-synthetics is best for models with strong negative curvature (−50°), the fit of synthetic *P*-waveforms at stations with high take-off angles and at azimuths that are roughly perpendicular to strike (e.g. CHTO, DGAR and XMIS) becomes significantly worse as the synthetic waveforms have the wrong initial polarity. The overall fit of all *P* and *SH* synthetics is good for models with geometries in the −40° to −10° curvature range. Due to the location of this event, much of the region lying to the south and within the teleseismic distance range is covered by ocean (Fig. 17a), therefore there are large (∼90°) azimuth gaps in the *S*-wave data-coverage. It would be preferable to have a more even distribution of station data, particularly for *SH*-waveform data, however there is strong evidence from the *SH*-waveform data that does exist (particularly from the along-strike stations to the north, and the one *SH*-station to the south, SYO)

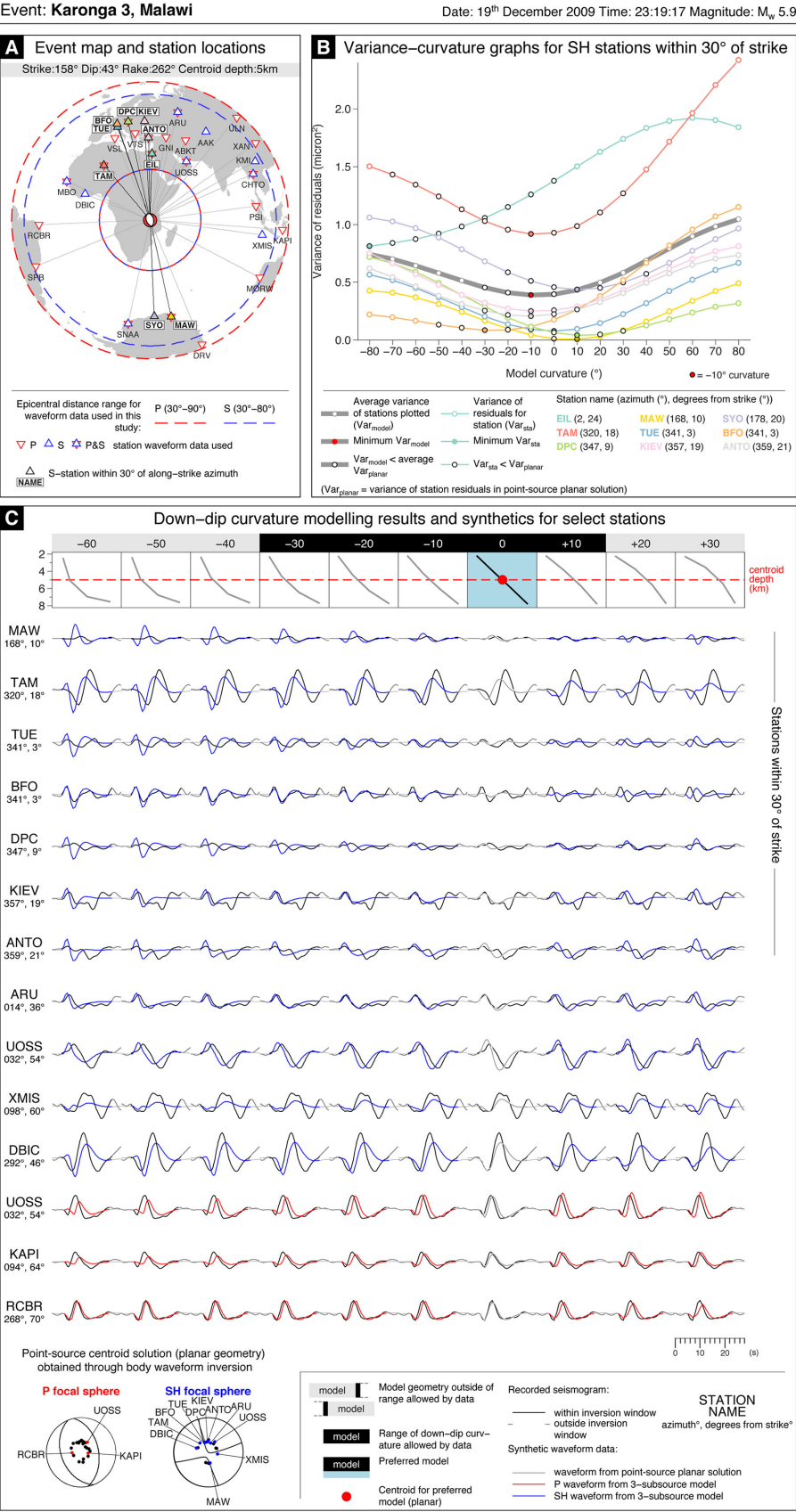**Figure 16.** Down-dip curvature modelling results for the 2009 December 19 Karonga earthquake. Caption as for Fig. 7.
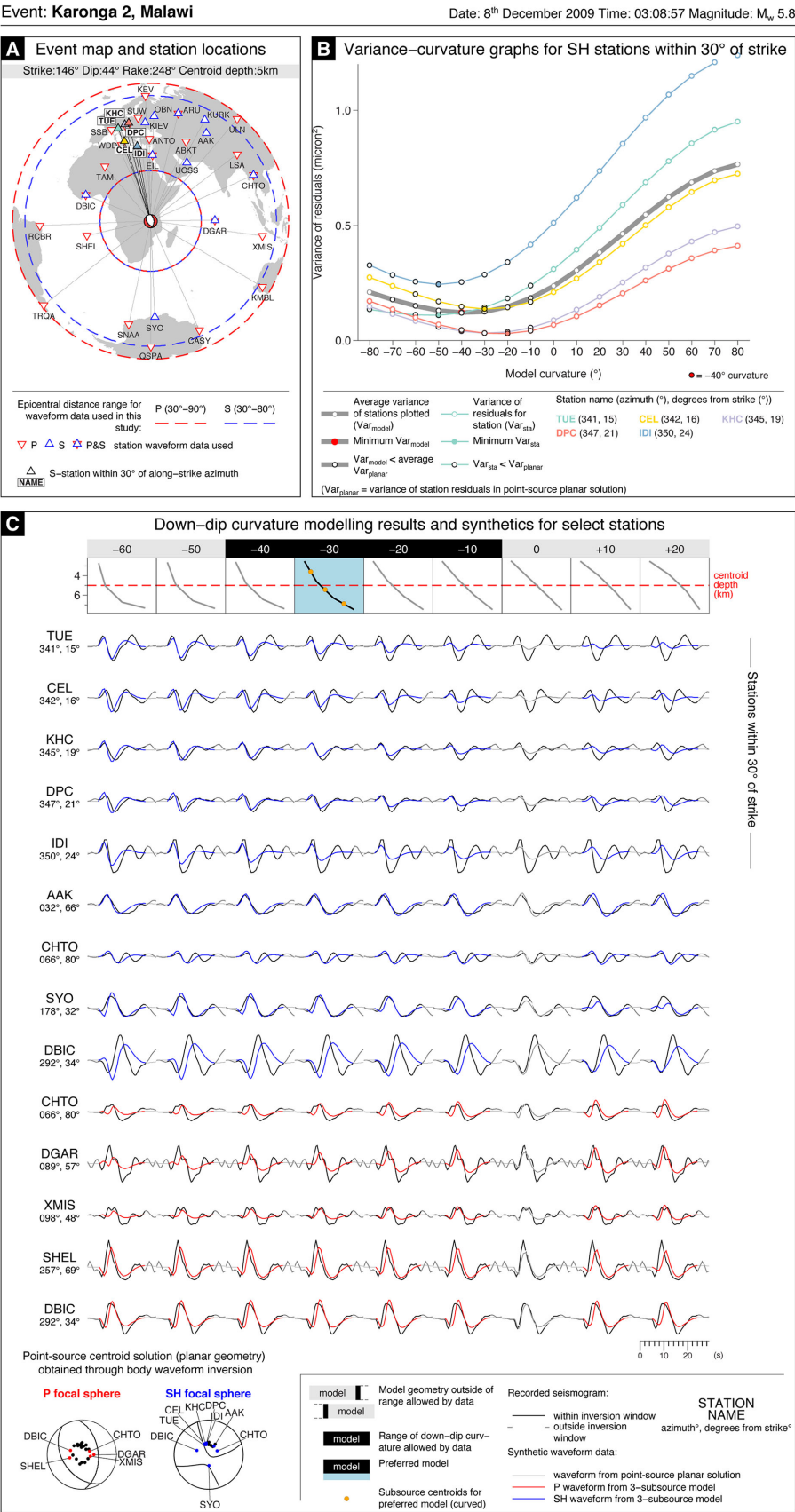
Figure 17. Down-dip curvature modelling results for the 2009 December 8 Karonga earthquake. Caption as for Fig. 7.

that this event ruptured a fault with negative down-dip curvature. From this evidence, and considering the fit to all available *P* and *SH* waveforms, our preferred model is −30° curvature.

2009 December 6 event. The planar solution from the body-waveform inversion generates *SH*-synthetics with similar waveform shapes and amplitudes to the observed models for the 9 stations at azimuths within 30° of strike (e.g. GNI, KBA; Fig. 18c). There is therefore no strong indication of down-dip curvature. However, the minimum-variance model for all but one station has a geometry with negative curvature (Fig. 18b), and models with some negative curvature (−30° to −10°) produce synthetics with similarly good wave shapes and amplitudes as the synthetics for the planar model. For all stations at azimuths >30° from strike, models with strong negative curvature yield synthetics with a better fit to the recorded *SH*-waveform than synthetics from the planar model, in terms of both the detail of waveform shape and the amplitude of the peak (e.g. UOSS −50°, DBIC −50°). At stations with high take-off angles and at azimuths that are perpendicular to strike (e.g. UOSS, PALK and SHEL), synthetic *P*-waveforms have small amplitudes and initial peaks with the wrong polarity compared to the recorded waveforms for models with −40° or more down-dip curvature, ruling out an extremely listric fault geometry. The fit synthetic *SH*-waveforms deteriorates for all stations for models with increasing positive curvature.

Due to the small size (M_w 5.7) and the location of this event, there is not a good azimuthal coverage of *SH*-stations at teleseismic distances (Fig. 18a), especially south of the event. There is a possibility that this event may have down-dip curvature, especially given its proximity to the 8th December event, however we are unable to constrain the geometry further than to say models with down-dip curvature in the range of −30° to +10° (including a planar geometry), give equally good overall fits to *P* and *SH* waveforms.

6 DISCUSSION

As described in the sections above, the down-dip curvature modelling results suggest that continental normal-faulting earthquakes that are large enough to penetrate to the bottom of the seismogenic layer rupture planar faults; most events showed no strong evidence for down-dip curvature, had dips between 30° and 60°, and could be constrained to be planar to within ±20°.

In both the Apennines and the Aegean, recent large normal-faulting earthquakes have generated very little surface rupture in regions with complex mapped faults. The rise of geodetic observational techniques (InSAR and GPS) has resulted in numerous studies that produced competing models of if, and how, the seismogenic slip is accommodated in the upper ≤1 km of crust, and on which faults. Fault plane measurements taken at the surface often show relatively steep dips (e.g. Jackson *et al.* 1982; Cello *et al.* 2000; Chiaraluce *et al.* 2005) compared to the source parameters estimated from seismology, resulting in authors describing faults as listric. However, this view is misleading. It is expected that normal fault planes steepen in upper ∼500 m as the rupture propagates towards a free surface, because this portion of the crust often fails in tension; exposed fault planes may also dip steeply due to unloading effects. This logic implies that there will be a significant underestimation of seismic hazard from surface studies, and that the structures accommodating slip in the near-surface do not reflect the geometry of the main seismogenic fault at depth. Fault planes may be expected to flatten at depth, if they detaches into a subhorizontal, rheologically weak unit. It is not unexpected that some seismo-

genic slip propagates onto these segments, however they generally do not make a significant contribution to the coseismic signal (e.g. Meyer *et al.* 1996). Indeed, our method will only resolve down-dip curvature if there is a significant moment contribution from these upper and lower portions of the fault plane. The advantage of the seismological technique presented in this paper is that we resolve the structure of the fault at depth, and on a gross scale, that is, the technique is only sensitive to the parts of the fault that are important in generating earthquakes and the picture is not obscured by the (entirely expected) complexity of surface faulting and deformation.

Partly due to the small magnitudes of the earthquakes, and partly due to the global distribution of seismometers, we have had very limited success in modelling oceanic earthquakes. For example, for events on the Mid-Atlantic Ridge there are large azimuthal gaps in station coverage at teleseismic distances, particularly along-strike to the north and south, as these regions are covered by ocean. Also, the amplitude of water multiples are often of a similar magnitude to the direct arrivals, which makes our analysis difficult. Both of the oceanic events that we studied are located in regions where there is no detailed bathymetry data to confirm whether or not core complexes (the uplifted, domed and corrugated footwalls of large-offset normal faults that expose mantle rocks) are present. It is impossible to distinguish on the basis of ocean floor bathymetry alone whether rift-parallel ridged relief forms as a result of simple domino-style extension and rotation of successive planar normal faults, or whether it is formed from the steep surface breakaways of listric detachment faults (Smith *et al.* 2008). Resolving the down-dip geometry of oceanic normal-faulting earthquakes offers a way to discriminate between models. Based on the observed waveforms, we inferred that both of the oceanic events we studied (Tables 1 and 2, and Appendix D in the Supporting Information) ruptured through the full seismogenic layer on planar faults.

In contrast to the majority of events we studied, there is strong evidence for listric down-dip curvature in some events from Tibet and East Africa. For events showing down-dip curvature, the maximum change in dip is 20°–30°. Although resolving this change in dip is a significant observation, it should be noted that the overall change is much less than that for the strongly listric fault geometries (≥50° change in dip) that are often drawn on geological cross-sections. The tightness of the constraints on the geometry is similar to the planar events, that is, within 10°–30° of the best-fitting model geometry. The ruptures we studied that displayed down-dip curvature occurred on antithetic faults, or minor faults within the hanging wall of a rift.

The location and the inferred depth extent of the rupture for both the 2004 and 2005 Zhongba (Tibet) events indicate that these earthquakes occurred on faults that cut through the hanging wall of a major rift-bounding normal fault. Our best-fit models, of −20° curvature, indicate the lower portion of the active faults may dip at ∼30°. This angle is similar to the ∼28° dip of the basal detachment Kapp *et al.* (2008) inferred to underlie the North Lunggar Rift, ∼100 km north-north-west of the Zhongba epicentres. The deeper structure of the South Lunggar Rift (where the Zhongba earthquakes were located) is not known. West of the Zhongba epicentres, the South Lunggar Detachment dips at 20° at the surface and exhumes mylonites and foliated rocks with a normal sense of shear (Styron *et al.* 2013). However, we have found no evidence for seismogenic slip on very low-angle normal faults (≤20° dip) in the Lunggar Rift, as has been debated for metamorphic core complexes in other parts of the world (Wernicke 1995; Axen 1999; Collettini 2011).

The 2009 Karonga earthquakes ruptured a series of ∼6–8 km long fault segments in the hanging wall of the Karonga Fault (which is
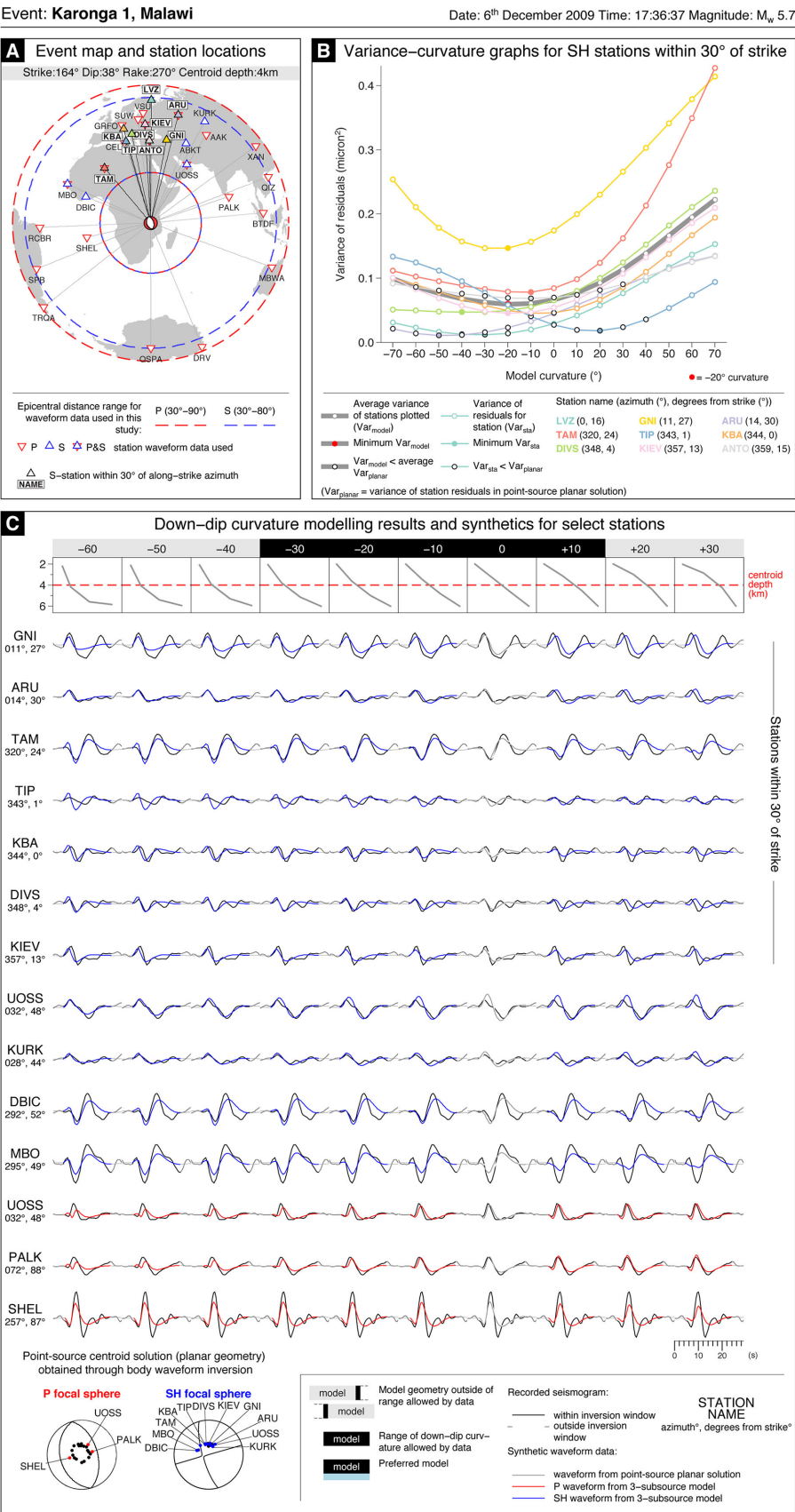
Figure 18. Down-dip curvature modelling results for the 2009 December 6 Karonga earthquake. Caption as for Fig. 7.

antithetic to the major basin-bounding Livingstone Fault), each with a small depth extent compared to the ≥40 km seismogenic thickness in this area (Foster & Jackson 1998; Ebinger *et al.* 1999; Maggi *et al.* 2000; Craig *et al.* 2011). For one event there is strong evidence of down-dip curvature, with a suggestion of possible curvature for a second. In the Karonga area the pre-existing structure is complex (Fig. 15b), and two opposing basement fabrics converge (Versfelt & Rosendahl 1989). It has been suggested that failure initiated on a favourably orientated pre-existing structure, and then migrated to adjacent planes of weakness as a result of static stress transfer (Fagereng 2013). Therefore it is possible that the varying down-dip geometries are an inherited feature, and result from the reactivation of old fabrics. However, the scale of the Livingstone Fault (i.e. the great width of the basin and the large topographic step resulting from the cumulative displacement across the fault), together with a low spreading rate (Saria *et al.* 2014) and long earthquake cycle, means that it must dominate the stress-state in the rift (Foster & Nimmo 1996; Ebinger *et al.* 1999), which may also be highly spatially variable. In this setting, it is perhaps not surprising that the minor faults are curved.

7 CONCLUSIONS

We have developed a new seismological technique to assess the down-dip shape of earthquake-generating faults through the analysis of body waveforms, and have successfully applied the technique to earthquakes in a variety of extensional environments. We have found that most normal-faulting earthquakes that rupture through the full seismogenic layer are planar and have dips of 30°–60°. There is evidence for faults with listric-sense down-dip curvature from earthquakes occurring in two regions; Tibet and East Africa. These ruptures occurred on antithetic faults, or minor faults within the hanging wall of a rift, and the change in dip across the fault plane is ∼30°.

ACKNOWLEDGEMENTS

REFERENCES

Amato, A. *et al.*, 1998. The 1997 Umbria-Marche, Italy, earthquake sequence: a first look at the main shocks and aftershocks, *Geophys. Res. Lett.,* **25**(15), 2861–2864.

Anzidei, M. *et al.*, 2009. Coseismic deformation of the destructive April 6, 2009 L'Aquila earthquake (central Italy) from GPS data, *Geophys. Res. Lett.,* **36**(17), L17307, doi:10.1029/2009GL039145.

Armijo, R., Tapponnier, P., Mercier, J.L. & Tong-Lin, H., 1986. Quaternary extension in southern Tibet: field observations and tectonic implications, *J. geophys. Res.,* **91**(B14), 13 803–13 872.

Armijo, R., Meyer, B., King, G.C.P., Rigo, A. & Papanastassiou, D. 1996. Quaternary evolution of the Corinth Rift and its implications for the Late Cenozoic evolution of the Aegean, *Geophys. J. Int.,* **126**, 11–53.

Atzori, S. *et al.*, 2009. Finite fault inversion of DInSAR coseismic displacement of the 2009 L'Aquila earthquake (central Italy), *Geophys. Res. Lett.,* **36**(15), doi:10.1029/2009GL039293.

Axen, G.J., 1999. Low-angle normal fault earthquakes and triggering, *Geophys. Res. Lett.,* **26**(24), 3693–3696.

Barba, S. & Basili, R., 2000. Analysis of seismological and geological observations for moderate-size earthquakes: the Colfiorito Fault System (Central Apennines, Italy), *Geophys. J. Int.,* **141**, 241–252.

Barchi, M.R. & Mirabella, F., 2009. The 1997–98 Umbria–Marche earthquake sequence: "geological" vs. "seismological" faults, *Tectonophysics,* **476**(1–2), 170–179.

Basili, R. & Meghraoui, M., 2001. Coseismic and postseismic displacements related with the 1997 Earthquake Sequence in Umbria-Marche (Central Italy), *Geophys. Res. Lett.,* **28**(14), 2695–2698.

Bellier, O. *et al.*, 2001. High slip rate for a low seismicity along the Palu-Koro active fault in central Sulawesi (Indonesia), *Terra Nova,* **13,** 463–470.

Bellier, O., Sébrier, M., Seward, D., Beaudouin, T., Villeneuve, M. & Putranto, E., 2006. Fission track and fault kinematics analyses for new insight into the Late Cenozoic tectonic regime changes in West-Central Sulawesi (Indonesia), *Tectonophysics,* **413**(3-4), 201–220.

Bergman, E.A. & Solomon, S.C., 1985. Earthquake source mechanisms from body-waveform inversion and intraplate tectonics in the northern Indian Ocean, *Phys. Earth planet. Inter.,* **40,** 1–23.

Bernard, P. *et al.*, 1997. The Ms=6.2, June 15, 1995 Aigion earthquake (Greece): evidence for low angle normal faulting in the Corinth rift, *J. Seismol.,* **1,** 131–250.

Bernard, P. *et al.*, 2006. Seismicity, deformation and seismic hazard in the western rift of Corinth: new insights from the Corinth Rift Laboratory (CRL), *Tectonophysics,* **426**(1-2), 7–30.

Biggs, J., Nissen, E., Craig, T.J., Jackson, J.A. & Robinson, D.P., 2010. Breaking up the hanging wall of a rift-border fault: the 2009 Karonga earthquakes, Malawi, *Geophys. Res. Lett.,* **37**(L11305), 1–5.

Boncio, P. & Lavecchia, G., 2000. A geological model for the Colfiorito earthquakes (September-October 1997, central Italy), *J. Seismol.,* **4,** 345–356.

Boncio, P., Pizzi, A., Brozzetti, F., Pomposo, G., Lavecchia, G., Di Naccio, D. & Ferrarini, F., 2010. Coseismic ground deformation of the 6 April 2009 L'Aquila earthquake (central Italy, M_w 6.3), *Geophys. Res. Lett.,* **37**(6), doi:10.1029/2010GL042807.

Bonini, L., Di Bucci, D., Toscani, G., Seno, S. & Valensise, G., 2014. On the complexity of surface ruptures during normal faulting earthquakes: excerpts from the 6 April 2009 L'Aquila (central Italy) earthquake (M_w 6.3), *Solid Earth,* **5**(1), 389–408.

Braunmiller, J. & Nábělek, J.L., 1996. Geometry of continental normal faults: seismological constraints, *J. geophys. Res.,* **101**(B2), 3045–3052.

Cattaneo, M. *et al.*, 2000. The 1997 Umbria-Marche (Italy) earthquake sequence: analysis of the data recorded by the local and temporary networks, *J. Seismol.,* **4,** 401–414.

Cello, G. *et al.*, 2000. Geological constraints for earthquake faulting studies in the Colfiorito area (central Italy), *J. Seismol.,* **4,** 357–364.

Cheloni, D. *et al.*, 2010. Coseismic and initial post-seismic slip of the 2009 M_w 6.3 L'Aquila earthquake, Italy, from GPS measurements, *Geophys. J. Int.,* **181**(3), 1–8.

Chiarabba, C. *et al.*, 2009. The 2009 L'Aquila (central Italy) M_w 6.3 earthquake: main shock and aftershocks, *Geophys. Res. Lett.,* **36**(18), L18308–6, doi:10.1029/2009GL039627.

Chiaraluce, L., 2003. Imaging the complexity of an active normal fault system: the 1997 Colfiorito (central Italy) case study, *J. geophys. Res.,* **108**(B6), 2294–19, doi:10.1029/2002JB002166.

Chiaraluce, L. *et al.*, 2004. Complex normal faulting in the Apennines thrust-and-fold belt: the 1997 seismic sequence in sentral Italy, *Bull. seism. Soc. Am.,* **94**(1), 99–116.

Chiaraluce, L., Barchi, M., Collettini, C., Mirabella, F. & Pucci, S., 2005. Connecting seismically active normal faults with Quaternary geological structures in a complex extensional environment: the Colfiorito 1997 case history (northern Apennines, Italy), *Tectonics,* **24**(1), doi:10.1029/2004TC001627.

Chiaraluce, L., Valoroso, L., Piccinini, D., Di Stefano, R. & De Gori, P., 2011. The anatomy of the 2009 L'Aquila normal fault system (central Italy) imaged by high resolution foreshock and aftershock locations, *J. geophys. Res.,* **116**(B12311), doi:10.1029/2011JB008352.

Cinti, F.R., Cucci, L., Marra, F. & Montone, P., 1999. The 1997 Umbria-Marche (Italy) earthquake sequence: relationship between ground deformation and seismogenic structure, *Geophys. Res. Lett.,* **26**(7), 895–898.

Cirella, A., Piatanesi, A., Cocco, M., Tinti, E., Scognamiglio, L., Michelini, A., Lomax, A. & Boschi, E., 2009. Rupture history of the 2009 L'Aquila (Italy) earthquake from non-linear joint inversion of strong motion and GPS data, *Geophys. Res. Lett.,* **36**(19), L19304, doi:10.1029/2009GL039795.

Clarke, P., Paradissis, D., Briole, P., England, P., Parsons, B.E., Billiris, H., Veis, G. & Ruegg, J.C., 1997. Geodetic investigation of the 13 May 1995 Kozani-Grevena (Greece) earthquake, *Geophys. Res. Lett.,* **24**(6), 707–710.

Coakley, B.J., Cochran, J.R. & Coch, 1998. Gravity evidence of very thin crust at the Gakkel Ridge (Arctic Ocean), *Earth planet. Sci. Lett.,* **162**, 81–95.

Cochran, J.R., 2003. The Gakkel Ridge: bathymetry, gravity anomalies, and crustal accretion at extremely slow spreading rates, *J. geophys. Res.,* **108**(B2), 2116, doi:10.1029/2002JB001830.

Collettini, C., 2011. The mechanical paradox of low-angle normal faults: current understanding and open questions, *Tectonophysics,* **510**(3-4), 253–268.

Collettini, C. & Sibson, R.H., 2001. Normal faults, normal friction?, *Geology,* **29**, 927–930.

Craig, T.J., Jackson, J.A. & Priestley, K., 2011. Earthquake distribution patterns in Africa: their relationship to variations in lithospheric and geological structure, and their rheological implications, *Geophys. J. Int.,* **185**, 403–434.

Craig, T.J., Copley, A. & Jackson, J.A., 2012. Thermal and tectonic consequences of India underthrusting Tibet, *Earth planet. Sci. Lett.,* **353–354**, 231–239.

Craig, T.J., Copley, A. & Jackson, J.A., 2014. A reassessment of outer-rise seismicity and its implications for the mechanics of oceanic lithosphere, *Geophys. J. Int.,* **197**(1), 63–89.

D'Agostino, N., Cheloni, D., Fornaro, G., Giuliani, R. & Reale, D., 2012. Space-time distribution of afterslip following the 2009 L'Aquila earthquake, *J. geophys. Res.,* **117**(B02402), doi:10.1029/2011JB008523.

Das, S. & Scholz, C.H., 1983. Why large earthquakes do not nucleate at shallow depths, *Nature,* **305**, 621–623.

deMartin, B.J., Sohn, R.A., Pablo Canales, J. & Humphris, S.E., 2007. Kinematics and geometry of active detachment faulting beneath the Trans-Atlantic Geotraverse (TAG) hydrothermal field on the Mid-Atlantic Ridge, *Geology,* **35**(8), 711–714.

De Martini, P.M., Pino, N.A., Valensise, G. & Mazza, S., 2003. Geodetic and seismologic evidence for slip variability along a blind normal fault in the Umbria-Marche 1997–1998 earthquakes (central Italy), *Geophys. J. Int.,* **155**, 819–829.

Demirci, A., Özden, S., Bekler, T., Kalafat, D. & Pınar, A., 2015. An active extensional deformation example: 19 May 2011 Simav earthquake ($M_w = 5.8$), Western Anatolia, Turkey, *J. Geophys. Eng.,* **12**, 552–565.

Deschamps, A. *et al.*, 2000. Spatio-temporal distribution of seismic activity during the Umbria-Marche crisis, 1997, *J. Seismol.,* **4**, 377–386.

Ebinger, C.J., Jackson, J.A., Foster, A.N. & Hayward, N.J., 1999. Extensional basin geometry and the elastic lithosphere, *Phil. Trans. R. Soc. A,* **357**, 741–765.

Ekström, G., Morelli, A., Boschi, E. & Dziewonski, A.M., 1998. Moment tensor analysis of the central Italy earthquake sequence of September-October 1997, *Geophys. Res. Lett.,* **25**(11), 1971–1974.

Elliott, J.R., Walters, R.J., England, P.C., Jackson, J.A., Li, Z. & Parsons, B.E., 2010. Extension on the Tibetan plateau: recent normal faulting measured by InSAR and body wave seismology, *Geophys. J. Int.,* **183**(2), 503–535.

EMERGEO Working, Group, 2009. Evidence for surface rupture associated with the M_w 6.3 L'Aquila earthquake sequence of April 2009 (central Italy), *Terra Nova,* **22**, 43–51.

Escartín, J., Smith, D.K., Cann, J., Schouten, H., Langmuir, C.H. & Escrig, S., 2008. Central role of detachment faults in accretion of slow-spreading oceanic lithosphere, *Nature,* **455**(7214), 790–794.

Eyidoğan, H. & Jackson, J.A., 1985. A seismological study of normal faulting in the Demirci, Alaşehir and Gediz earthquakes of 1969-70 in western Turkey: implications for the nature and geometry of deformation in the continental crust, *Geophys. J. Int.,* **81**(3), 569–607.

Fagereng, Å., 2013. Fault segmentation, deep rift earthquakes and crustal rheology: insights from the 2009 Karonga sequence and seismicity in the Rukwa–Malawi rift zone, *Tectonophysics,* **601**(C), 216–225.

Falcucci, E. *et al.*, 2009. The Paganica Fault and surface coseismic ruptures caused by the 6 April 2009 earthquake (L'Aquila, central Italy), *Seismol. Res. Lett.,* **80**(6), 940–950.

Flannery, J.W. & Rosendahl, B.R., 2009. The seismic stratigraphy of Lake Malawi, Africa: implications for interpreting geological processes in lacustrine rifts, *J. Afr. Earth Sci.,* **10**(3), 519–548.

Foster, A. & Nimmo, F., 1996. Comparisons between the rift systems of East Africa, Earth and Beta Regio, Venus, *Earth planet. Sci. Lett.,* **143**, 183–195.

Foster, A.N. & Jackson, J.A., 1998. Source parameters of large African earthquakes: implications for crustal rheology and regional kinematics, *Geophys. J. Int.,* **134**, 422–448.

Fredrich, J., McCaffrey, R. & Denham, D., 1988. Source parameters of seven large australian earthquakes determined by body waveform inversion, *Geophys. J.,* **95**, 1–13.

Geller, R.J., 1976. Scaling relations for earthquake source parameters and magnitudes, *Bull. seism. Soc. Am.,* **66**(5), 1501–1523.

Hall, R., 2002. Cenozoic geological and plate tectonic evolution of SE Asia and the SW Pacific: computer-based reconstructions, model and animations, *J. Asian Earth Sci.,* **20**(4), 353–431.

Hamiel, Y., Baer, G., Kalindekafe, L., Dombola, K. & Chindandali, P., 2012. Seismic and aseismic slip evolution and deformation associated with the 2009-2010 northern Malawi earthquake swarm, East African Rift, *Geophys. J. Int.,* **191**, 898–908.

Hartzell, S.H. & Heaton, T.H., 1983. Inversion of strong ground motion and teleseismic waveform data for the fault rupture history of the 1979 Imperial Valley, California, earthquake, *Bull. seism. Soc. Am.,* **73**(6), 1553–1583.

Hatzfeld, D., Karakostas, V., Ziazia, M., Selvaggi, G., Leborgne, S., Berge, C. & Makropoulos, K., 1998. The Kozani-Grevena (Greece) earthquake of May 13, 1995, a seismological study, *J. Geodyn.,* **26**(2-4), 245–254.

Hatzfeld, D., Karakostas, V., Ziazia, M., Kassaras, I., Papadimitriou, E., Makropoulos, K., Voulgaris, N. & Papaioannou, C., 2000. Microseismicity and faulting geometry in the Gulf of Corinth (Greece), *Geophys. J. Int.,* **141**, 438–456.

Herrmann, R.B., Malagnini, L. & Munafo, I., 2011. Regional Moment Tensors of the 2009 L'Aquila Earthquake Sequence, *Bull. seism. Soc. Am.,* **101**(3), 975–993.

Hunstad, I., Anzidei, M., Cocco, M., Baldi, P., Galvani, A. & Pesci, A., 1999. Modelling coseismic displacements during the 1997 Umbria-Marche earthquake (central Italy), *Geophys. J. Int.,* **139**, 283–295.

Ishii, M., Shearer, P.M., Houston, H. & Vidale, J.E., 2005. Extent, duration and speed of the 2004 Sumatra–Andaman earthquake imaged by the Hi-Net array, *Nature,* **435**, 933–936.

Jackson, J.A. & Blenkinsop, T., 1997. The Bilila-Mtakataka fault in Malawi: an active, 100 km long, normal fault segment in thick seismogenic crust, *Tectonics,* **16**(1), 137–150.

Jackson, J.A. & McKenzie, D., 1983. The geometrical evolution of normal fault systems, *J. Struct. Geol.,* **5**(5), 471–482.

Jackson, J.A. & White, N.J., 1989. Normal faulting in the upper continental crust: observations from regions of active extension, *J. Struct. Geol.,* **11**(1/2), 15–36.

Jackson, J.A., Gagnepain, J., Houseman, G., King, G.C.P., Papadimitriou, P., Soufleris, C. & Virieux, J., 1982. Seismicity, normal faulting, and the geomorphological development of the Gulf of Corinth (Greece): the Corinth earthquakes of February and March 1981, *Earth planet. Sci. Lett.,* **57**, 377–397.

Jakobsson, M. *et al.*, 2012. The International Bathymetric Chart of the Arctic Ocean (IBCAO) Version 3.0, *Geophys. Res. Lett.,* **39**(L12609), doi:10.1029/2012GL052219.

Ji, C., Helmberger, D.V., Wald, D.J. & Ma, K.-F., 2003. Slip history and dynamic implications of the 1999 Chi-Chi, Taiwan, earthquake, *J. geophys. Res.,* **108**(B9), 2412, doi:10.1029/2002JB001764.

Kapp, P., Taylor, M., Stockli, D. & Ding, L., 2008. Development of active low-angle normal fault systems during orogenic collapse: insight from Tibet, *Geology,* **36**(1), 7–10.

Karasözen, E., Nissen, E., Bergman, E.A., Johnson, K.L. & Walters, R.J., 2016. Normal faulting in the Simav graben of western Turkey reassessed with calibrated earthquake relocations, *J. geophys. Res.,* **121**(6), 4553–4574.

Lundgren, P. & Stramondo, S., 2002. Slip distribution of the 1997 Umbria-Marche earthquake sequence: joint inversion of GPS and synthetic aperture radar interferometry data, *J. geophys. Res.,* **107**(B11), 2316, doi:10.1029/2000JB000103.

Macheyeki, A.S. *et al.*, 2015. Active fault mapping in Karonga-Malawi after the December 19, 2009 Ms 6.2 seismic event, *J. Afr. Earth Sci.,* **102**(C), 233–246.

MacLeod, C.J., Searle, R.C., Murton, B.J., Casey, J.F., Mallows, C., Unsworth, S.C., Achenbach, K.L. & Harris, M., 2009. Life cycle of oceanic core complexes, *Earth planet. Sci. Lett.,* **287**(3-4), 333–344.

Maggi, A., Jackson, J.A., Priestley, K. & Baker, C., 2000. A re-assessment of focal depth distributions in southern Iran, the Tien Shan and northern India: do earthquakes really occur in the continental mantle? *Geophys. J. Int.,* **143**, 629–661.

Mai, P.M., Spudich, P. & Boatwright, J., 2005. Hypocenter locations in finite-source rupture models, *Bull. seism. Soc. Am.,* **95**(3), 965–980.

McCaffrey, R. & Abers, G., 1988. SYN3: a program for inversion of teleseismic body wave forms on microcomputers, *Tech. rep.*, Air Force Geophysics Laboratory.

McCaffrey, R., Zwick, P. & Abers, G., 1991. SYN4 Program, *IASPEI Softw. Libr.,* **3**, 81–166.

McGuire, J.J., Zhao, L. & Jordan, T.H., 2002. Predominance of unilateral rupture for a global catalog of large earthquakes, *Bull. seism. Soc. Am.,* **92**(8), 3309–3317.

Meyer, B. *et al.*, 1996. The 1995 Grevena (northern Greece) earthquake: fault model constrained with tectonic observations and SAR interferometry, *Geophys. Res. Lett.,* **23**(19), 2677–2680.

Middleton, T.A. & Copley, A., 2013. Constraining fault friction by re-examining earthquake nodal plane dips, *Geophys. J. Int.,* **196**(2), 671–680.

Mirabella, F., Barchi, M., Lupattelli, A., Stucchi, E. & Ciaccio, M.G., 2008. Insights on the seismogenic layer thickness from the upper crust structure of the Umbria-Marche Apennines (central Italy), *Tectonics,* **27**(TC1010).

Molnar, P. & Lyon-Caen, H., 1989. Fault plane solutions of earthquakes and active tectonics of the Tibetan Plateau and its margins, *Geophys. J. Int.,* **99**, 123–153.

Morelli, A., Ekström, G. & Olivieri, M., 2000. Source properties of the 1997–98 Central Italy earthquake sequence from inversion of long-period and broad-band seismograms, *J. Seismol.,* **4**, 365–375.

Nábělek, J.L., 1984. rmination of earthquake source parameters from inversion of body waves, *PhD thesis*, MIT, Dept. of Earth, Atmospheric and Planetary Sciences.

Nelson, M.R., McCaffrey, R. & Molnar, P., 1987. Source parameters for 11 earthquakes in the Tien Shan, central Asia, determined by P and SH waveform inversion, *J. geophys. Res.,* **92**(B12), 12 629–12 648.

Pondrelli, S., Salimbeni, S., Morelli, A., EkstrÃ,m G., Olivieri, M. & Boschi, E., 2010. Seismic moment tensors of the April 2009, L'Aquila (Central Italy), earthquake sequence, *Geophys. J. Int.,* **180**(1), 238–242.

Resor, P.G., Pollard, D.D., Wright, T.J. & Beroza, G.C., 2005. Integrating high-precision aftershock locations and geodetic observations to model coseismic deformation associated with the 1995 Kozani-Grevena earthquake, Greece, *J. geophys. Res.,* **110**(B09402), 2156–2202.

Rietbrock, A., Tiberi, C., Scherbaum, F. & Lyon-Caen, H., 1996. Seismic slip on a low angle normal fault in the Gulf of Corinth: evidence from high-resolution cluster analysis of microearthquakes, *Geophys. Res. Lett.,* **23**(14), 1817–1820.

Rigo, A., Lyon-Caen, H., Armijo, R., Deschamps, A., Hatzfeld, D., Makropoulos, K., Papadimitriou, P. & Kassaras, I., 1996. A microseismic study in the western part of the Gulf of Corinth (Greece): implications for largescale normal faulting mechanisms, *Geophys. J. Int.,* **126**, 663–688.

Rigo, A., Chabalier, J.-B.d., Meyer, B. & Armijo, R., 2004. The 1995 Kozani-Grevena (northern Greece) earthquake revisited: an improved faulting model from synthetic aperture radar interferometry, *Geophys. J. Int.,* **157**(2), 727–736.

Roberts, G.P. & Michetti, A.M., 2004. Spatial and temporal variations in growth rates along active normal fault systems: an example from The Lazio–Abruzzo Apennines, central Italy, *J. Struct. Geol.,* **26**(2), 339–376.

Salvi, S. *et al.*, 2000. Modeling coseismic displacements resulting from SAR interferometry and GPS measurements during the 1997 Umbria-Marche seismic sequence, *J. Seismol.,* **4**, 479–499.

Saria, E., Calais, E., Stamps, D.S., Delvaux, D. & Hartnady, C. J.H., 2014. Present-day kinematics of the East African Rift, *J. geophys. Res.,* **119**(4), 3584–3600.

Scholz, C.H., 1982. Scaling laws for large earthquakes: consequences for physical models, *Bull. seism. Soc. Am.,* **72**(1), 1–14.

Scholz, C.H., 1998. Earthquakes and friction laws, *Nature,* **391**, 37–42.

Scognamiglio, L., Tinti, E., Michelini, A., Dreger, D.S., Cirella, A., Cocco, M., Mazza, S. & Piatanesi, A., 2010. Fast determination of moment tensors and rupture history: what has been learned from the 6 April 2009 L'Aquila earthquake sequence, *Seismol. Res. Lett.,* **81**(6), 892–906.

Serpelloni, E., Anderlini, L. & Belardinelli, M.E., 2011. Fault geometry, coseismic-slip distribution and Coulomb stress change associated with the 2009 April 6, M_w 6.3, L'Aquila earthquake from inversion of GPS displacements, *Geophys. J. Int.,* **188**(2), 473–489.

Seyitoglu, G., 1997. The Simav Graben: an example of young E-W trending structures in Late Cenozoic extensional system of Western Turkey, *Turk. J. Earth Sci.,* **6**, 135–141.

Sibson, R.H., 1984. Roughness at the base of the seismogenic zone: contributing factors, *J. geophys. Res.,* **89**(B7), 5791–5799.

Sibson, R.H., 1985. A note on fault reactivation, *J. Struct. Geol.,* **7**(6), 751–754.

Sloan, R.A., Jackson, J.A., McKenzie, D. & Priestley, K., 2011. Earthquake depth distributions in central Asia, and their relations with lithosphere thickness, shortening and extension, *Geophys. J. Int.,* **185**(1), 1–29.

Smith, D.K., Escartín, J., Schouten, H. & Cann, J.R., 2008. Fault rotation and core complex formation: significant processes in seafloor formation at slow-spreading mid-ocean ridges (Mid-Atlantic Ridge, 13°–15°N), *Geochem. Geophys. Geosyst.,* **9**(3), doi:10.1029/2007GC001699.

Smith, D.K. *et al.*, 2014. Development and evolution of detachment faulting along 50 km of the Mid-Atlantic Ridge near 16.5°N, *Geochem. Geophys. Geosyst.,* **15**(12), 4692–4711.

Socquet, A., Simons, W., Vigny, C., McCaffrey, R., Subarya, C., Sarsito, D., Ambrosius, B. & Spakman, W., 2006. Microblock rotations and fault coupling in SE Asia triple junction (Sulawesi, Indonesia) from GPS and earthquake slip vector data, *J. geophys. Res.,* **111**(B08409), doi:10.1029/2005JB003963.

Spudich, P. & Cranswick, E., 1984. Direct observation of rupture propagation during the 1979 Imperial Valley earthquake using a short baseline accelerometer array, *Bull. seism. Soc. Am.,* **74**(6), 2083–2114.

Stefatos, A., Papatheodorou, G., Ferentinos, G., Leeder, M. & Collier, R., 2002. Seismic reflection imaging of offshore faults in the Gulf of Corinth: their seismotectonic significance, *Basin Res.,* **14**, 487–502.

Stramondo, S. *et al.*, 1999. The September 26, 1997 Colfiorito, Italy, earthquakes: modeled coseismic surface displacement from SAR interferometry and GPS, *Geophys. Res. Lett.,* **26**(7), 883–886.

Styron, R.H. *et al.*, 2013. Miocene initiation and acceleration of extension in the South Lunggar rift, western Tibet: evolution of an active detachment system from structural mapping and (U-Th)/He thermochronology, *Tectonics,* **32**, 880–907.

Taymaz, T., Jackson, J.A. & Westaway, R. W.C., 1990. Earthquake mechanisms in the Hellenic Trench near Crete, *Geophys. J. Int.,* **102**, 695–731.

Taymaz, T., Jackson, J.A. & McKenzie, D., 1991. Active tectonics of the north and central Aegean Sea, *Geophys. J. Int.,* **106**(2), 433–490.

Valoroso, L., Chiaraluce, L., Piccinini, D., Di Stefano, R., Schaff, D. & Waldhauser, F., 2013. Radiography of a normal fault system by 64,000 high-precision earthquake locations: the 2009 L'Aquila (central Italy) case study, *J. geophys. Res.,* **118**(3), 1156–1176.

Velasco, M.S., Bennett, R.A., Johnson, R.A. & Hreinsdóttir, S., 2010. Sub-surface fault geometries and crustal extension in the eastern Basin and Range Province, western U.S., *Tectonophysics,* **488**(1-4), 131–142.

Versfelt, J. & Rosendahl, B.R., 1989. Relationships between pre-rift structure and rift architecture in Lakes Tanganyika and Malawi, East Africa, *Nature,* **337**, 354–357.

Vittori, E., Delvaux, D. & Kervyn, F., 1997. Kanda Fault: a major seismo-genic element west of the Rukwa Rift (Tanzania, East Africa), *J. Geodyn.,* **24**(1-4), 139–153.

Vittori, T. *et al.*, 2000. Ground effects and surface faulting in the September-October 1997 Umbria-Marche (Central Italy) seismic sequence, *J. Geodyn.,* **29**(3-5), 535–564.

Wald, D.J. & Heaton, T.H., 1994. Spatial and Temporal Distribution of Slip for the 1992 Landers, California, Earthquake, *Bull. seism. Soc. Am.,* **84**(3), 668–691.

Walters, R.J. *et al.*, 2009. The 2009 L'Aquila earthquake (central Italy): a source mechanism and implications for seismic hazard, *Geophys. Res. Lett.,* **36**(L17312), doi:10.1029/2009GL039337.

Wernicke, B.P., 1995. Low-angle normal faults and seismicity: a review, *J. geophys. Res.,* **100**(B10), 20 159–20 174.

Westaway, R., 1990. Block rotation in western Turkey: 1. Observational evidence, *J. geophys. Res.,* **95**(B12), 19857–19884.

Zeng, Y. & Chen, C.-H., 2001. Fault rupture process of the 20 September 1999 Chi-Chi, Taiwan, earthquake, *Bull. seism. Soc. Am.,* **91**(5), 1088–1098.

Zwick, P., McCaffrey, R. & Abers, G., 1994. MT5 Program, *IASPEI Softw. Libr.,* **4**.

SUPPORTING INFORMATION

Supplementary data are available at *GJI* online.

CurvePaper_GJIformat_appendices2.pdf

Please note: Oxford University Press is not responsible for the content or functionality of any supporting materials supplied by the authors. Any queries (other than missing material) should be directed to the corresponding author for the paper.